A theoretical study of parietal vortex shedding in Taylor–Culick flow via linear stability analysis

Yang Li 李阳 ,[1] Zhuopu Wang 王琢璞 ,[1, a)] Peijin Liu 刘佩进 ,[1] Wei He 何伟 ,[2] and Larry K.B. Li[3]
[1)]*Science and Technology on Combustion, Internal Flow and Thermo-Structure Laboratory, Northwestern Polytechnical University, Xi'an, 710072, Shaanxi, China*
[2)]*School of Engineering, University of Liverpool, Brownlow Hill, England L69 3GH, United Kingdom.*
[3)]*Department of Mechanical and Aerospace Engineering, The Hong Kong University of Science and Technology, Clear Water Bay, Hong Kong*

(Dated: 9 September 2020)

In this theoretical study, we use linear stability analysis to investigate the cause of parietal vortex shedding in Taylor–Culick flow, which is representative of the flow in solid rocket motors. We focus on the effects of the lateral-injection Reynolds number and the length-to-radius ratio of the combustion chamber. Through a comparison with pipe flow, we find that flow turning is a major contributor to parietal vortex shedding. We explore the role of amphidromic points and find that they can divide the flow field into two distinct regions, an outer region with strong perturbations and an inner region with weak perturbations. In the outer region, we find that the velocity perturbations develop advection patterns with axial (streamwise) periodicity, while the pressure perturbations induce flow gradients that enhance shear stresses. Collectively these effects are thought to combine to induce parietal vortex shedding in solid rocket motors.

I. INTRODUCTION

In solid rocket motors (SRMs), especially those with high length-to-radius ratios, vortex shedding can be an important mechanism by which self-excited pressure oscillations arise in combustion chambers. This has therefore prompted numerous studies on the characterization, prediction and control of vortex shedding in SRM chambers, in an effort to better understand unsteady multi-scale phenomena such as combustion instabilities and transition. In seminal work, Flandro[1] proposed that vortex shedding could couple with acoustic disturbances in the chamber, producing large-amplitude pressure oscillations. Several experiments[2,3] have since confirmed the importance of vortex shedding, particularly the vortex structure and dynamics, in producing self-excited pressure oscillations. Early studies on the mechanisms of vortex shedding in SRMs focused mainly on the shear layers produced by the non-smooth or discontinuous geometry of the propellant surface, such as the flow behind backward-facing steps (which is affected by the angle of the propellant ends, and by the cavity between the segments) and the flow behind obstacle structures (which is affected by the inhibitor ring situated between segments protruding from the propellant surface during SRM burning)[4]. Vortices, however, can also arise without backward-facing steps or obstacle structures, through an alternative mechanism known as parietal vortex shedding.

The importance of parietal vortex shedding was revealed by Lupoglazoff and Vuillot[5] in their numerical simulations of SRM flow using the unsteady 2D compressible Navier–Stokes equations. This study was later followed by several supporting experiments. For example, Avalon et al.[6] used planar laser-induced fluorescence to examine the 2D lateral mass injection of porous materials in the VECLA facility. The wave pattern at the downstream end of the channel domain was measured for a fixed channel height. The frequency of vortex shedding was found to be equal to one of the longitudinal acoustic eigenfrequencies of the channel, highlighting the importance of interactions between parietal vortex shedding and the natural acoustic modes of the system. In further experiments, Avalon et al.[7] used the VALDO facility, which consists of a long cylinder with lateral mass injection at the extension surface and which can be thought of as a 3D version of the 2D VECLA facility[6]. Parietal vortex shedding was also observed in this 3D facility, consistent with the results of bi-global stability analysis. These findings show that parietal vortex shedding is a key flow feature in SRM chambers and has been well established via numerical simulations and experiments.

The physical cause of parietal vortex shedding has been the subject of numerous studies, particularly those involving theoretical analysis[8–10]. Traditional vortex theory, as applied to SRMs, tends to focus on the interaction between fully developed vortices and acoustic disturbances, but relatively little is known about the cause of parietal vortex shedding. Background noise is thought to be a key driving mechanism[11], as previous work has shown that accurate numerical simulation of parietal vortex shedding requires the addition of white noise[5]. Using large-eddy simulations (LES), Apte and Yang[12] investigated the complete laminar-to-turbulent transition process and found that it occurred at mid-downstream locations. They also found that, as the Reynolds number increased, the region of peak turbulence intensity shifted downstream. The role of lateral mass injection was found to be particularly influential in reducing wall shear stresses. However, because the LES of Apte and Yang[12] did not reveal evidence of vortex stretching, further analysis of the full effect of lateral mass injection is required. In particular, Apte and Yang[12] used a semi-empirical model to capture the effect of unresolved scales and applied white noise to capture the effect of surface roughness and pseudo-turbulence. The resultant predictions may be compared with those from hydrodynamic stability analysis[13]. Using numerical simulations with a time-dependent turbulence model, Kourta[14] showed

[a)]Electronic mail: zpwang@nwpu.edu.cn

that white noise and turbulence are not always necessary for the onset of parietal vortex shedding, implying that an intrinsic mechanism for flow instability is operative. By performing a sub-grid stability analysis, Boyer et al.[15,16] showed that the instability frequency calculated theoretically was consistent with the frequency of parietal vortex shedding observed experimentally. They were able to relate the cause of vortex generation to singular points in the perturbed velocity field. Such points are often referred to as amphidromic points.

As the above review has shown, in flows with lateral mass injection (e.g. SRM flows), parietal vortex shedding is believed to arise from an intrinsic instability mechanism, which is thought to be independent of the presence of white noise and external perturbations. In this theoretical study, we use linear stability analysis to better understand the mechanism responsible for parietal vortex shedding. First we examine the effect of lateral mass injection by comparing it with that of head mass injection, as modeled with simple pipe flow. Then we consider the specific characteristics of the flow field produced by lateral mass injection, with a focus on the creation of amphidromic points. We relate such singular points, obtained via analysis of the perturbation variables, to the characteristics of spatially propagating perturbations in the flow. From these observations, we propose a theoretical explanation for the generation of parietal vortex shedding, contributing to a better understanding of unsteady multi-scale combustion phenomena in SRMs[17–19].

This paper is organized as follows. We present the problem configuration and governing equations in Section II, and then numerically validate the theoretical framework in Section III. In Section IV, we examine the hydrodynamic stability of Taylor–Culick flow under various conditions and compare its eigenvalue spectrum with that of pipe flow. In Section V, we perform a bi-global stability analysis and investigate the effects of flow turning by comparing Taylor–Culick flow with pipe flow. In Section VI, we conclude by highlighting the key findings and implications of this study.

II. PROBLEM CONFIGURATION

A. Equations of motion

The geometric configuration under study is classic Taylor–Culick flow[16], which features a cylindrical axisymmetric flow field with constant lateral velocity injection, as shown in Fig. 1a. The flow field is thus characterized by the degree of lateral injection. For comparison, a pipe flow model with constant head injection is also considered, as shown in Fig. 1b.

The flow in an SRM chamber is at a relatively low speed (Mach number < 0.3), so the incompressible flow assumption is adopted[20]. The reference values for length, velocity, time and pressure are chosen as R, V_{inj}, R/V_{inj} and ρV_{inj}^2, respectively. Here R is the chamber radius, V_{inj} is the lateral/head injection velocity, and ρ is the fluid density. With these reference values, the non-dimensional form of the governing equations becomes[21],

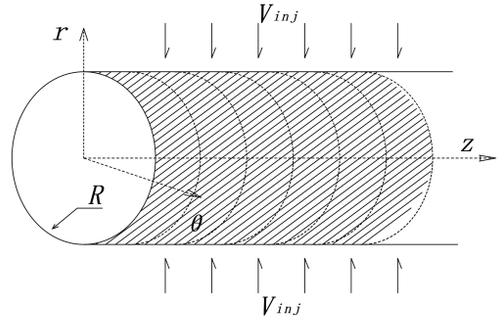

(a) Taylor–Culick flow

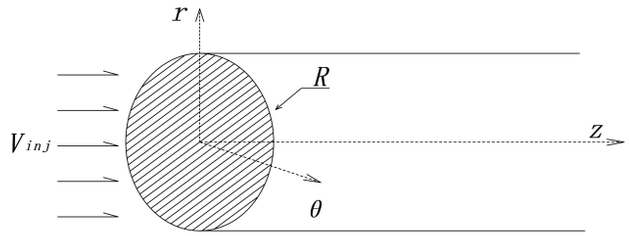

(b) Pipe flow

FIG. 1: Schematic diagram of Taylor-Culick flow and pipe flow models:(a)Taylor-Culick flow model simulating nozzleless rocket motor with lateral injection;(b)pipe flow.

$$\begin{cases} \nabla \cdot U = 0, \\ \dfrac{\partial U}{\partial t} + (U \cdot \nabla)U + \nabla P = \dfrac{1}{Re}\Delta U, \end{cases} \tag{1}$$

where $U = (U_r, U_\theta, U_z)$ is the velocity field, P is the pressure, and $Re \equiv RV_{\text{inj}}/\nu$ is the Reynolds number based on the injection velocity, where ν is the kinematic viscosity of the fluid.

In linear stability analysis[22], the flow field (U, P) can be decomposed into two parts, the mean and the perturbation, denoted respectively by an overbar and by a prime,

$$\begin{cases} U = \bar{U} + u', \\ P = \bar{P} + p'. \end{cases} \tag{2}$$

Substituting Eq. (2) into Eq. (1) and discarding the higher-order terms leads to a linearized system for the perturbations,

$$\begin{cases} \nabla \cdot u' = 0, \\ \dfrac{\partial u'}{\partial t} + (\bar{U} \cdot \nabla)u' + (u' \cdot \nabla)\bar{U} + \nabla p' = \dfrac{1}{Re}\Delta u'. \end{cases} \tag{3}$$

In bi-global stability analysis[10], perturbations are assumed to have the following form,

$$q' = \hat{q}(r,z)e^{i(m\theta-\omega t)}, \tag{4}$$

where $q' = [u'_r, u'_\theta, u'_z, p']$. The azimuthal wavenumber m is assumed to be an integer, which makes the problem easier to decompose. The dynamics of the perturbations is determined by the complex frequency $\omega = \omega_r + \omega_i i$. The real part ω_r is the dimensionless angular frequency, and the imaginary part ω_i is the growth rate of the perturbations. A positive (negative) ω_i implies that the perturbations grow (decay) exponentially in time. Substituting Eq. (4) into Eq. (3) yields a generalized eigenvalue problem,

$$A\hat{q} = i\omega \cdot B\hat{q}. \tag{5}$$

The boundary conditions are found by normalizing the flow conditions and by separating the perturbation variables, which are chosen to allow for the calculation of a well-posed adjoint stability problem[16]. The head and axis are wall and symmetry boundary conditions, respectively. The lateral injection inlet has a constant velocity and is assumed to have no external disturbances. A natural free-stress condition is imposed at the outlet boundary,

$$-\frac{1}{Re}\nabla u' \cdot n + p' \cdot n = 0, \tag{6}$$

where n is the outward normal vector at the outlet boundary.

III. VALIDATION

To validate the present theoretical framework, we compute the eigenvalue spectrum for Taylor–Culick flow at the same conditions ($Re = 2200$ and $m = 0$) as those in the theoretical study of Boyer et al.[16]. The results are shown in Fig. 2, where the red markers represent the eigenvalues calculated here, and the blue markers represent the eigenvalues reported by Boyer et al.[16]. It can be seen that there is reasonable agreement in the overall trends of the eigenvalues, although systematic discrepancies (offsets) can be identified between the two data sets. These discrepancies, which grow in magnitude as ω_r increases, are attributed to differences in the number of grid cells, an effect that has been investigated in detail in our recent work[21]. In particular, it was found that the grid dependence of the stability of Taylor–Culick flow is partly determined by a structural error rule for the eigenvalue spectra[21]. Therefore, the overall error can be reduced by following such a rule. For this reason, we use a grid size of 30×250 in the rest of this study.

As a further validation test, the predictions of the present linear stability analysis are compared with those of computational fluid dynamics (CFD) simulations. It should be noted that, in this comparison, the physical frequency (f in Hz) can be calculated from the dimensionless angular frequency (ω_r) via,

$$f = \frac{V_{\text{inj}}}{2\pi r}\omega_r. \tag{7}$$

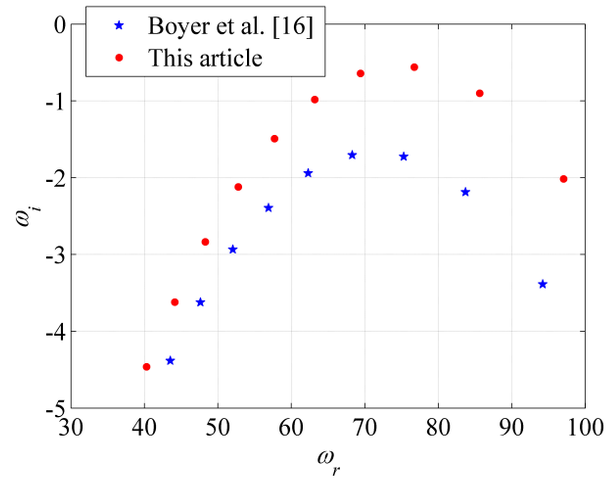

FIG. 2: Comparison of eigenvalue spectra for Taylor–Culick flow: the present study vs. Boyer et al.[16].

Table I lists the operating conditions of the validation cases from the literature[12,16], while Table II compares the frequency predictions made here against those made by the LES of Apte and Yang[12]. The data in Table II are extracted from the local peaks (P_1 and P_2) in the eigenvalue spectra of Fig. 3, which are calculated for Taylor–Culick flow at two representative values of the length-to-radius ratio: $L/r = 15$ and 24. The corresponding frequencies predicted by LES[12] are determined by computing the power spectra of the flow fluctuations. From Table II, it can be seen that the theoretical and numerical data match very well in terms of the P_2 frequency (differences of under 1.4%), but match less well in terms of the P_1 frequency (differences of around 14%).

The difference in the P_1 frequency prediction can be understood more easily by inspecting Fig. 3. At $L/r = 15$ (Fig. 3a), the local peak at P_1 in the eigenvalue spectrum corresponds to a stable mode, as evidenced by the negative value of ω_i. When L/r increases to 24 (Fig. 3b), however, this peak settles onto the background spectrum, making it difficult to identify with confidence. In the LES of Apte and Yang[12], the P_1 mode can still be identified, presumably owing to the presence of external disturbances such as white background noise. For both $L/r = 15$ and 24, our linear stability analysis predicts that the P_2 mode exhibits a positive value of ω_i, indicating that this mode is intrinsically hydrodynamically unstable. The fact that there is excellent agreement in the P_2 frequency between the present analysis and the LES of Apte and Yang[12] shows that we are able to accurately capture the dominant unstable mode in Taylor–Culick flow.

IV. STABILITY ANALYSIS OF TAYLOR–CULICK FLOW

A. Effect of L/r, Re and m

Fig. 4 shows the eigenvalue spectra for Taylor–Culick flow at $Re = 2500$ and four different values of the length-to-radius

TABLE I: Operating conditions and fluid properties for validation cases.

	Re	V_{inj} (1)	L (m)	R (m)	L/r	Fluid	μ (Pa · s)	T (K)
Boyer et al.[16]	2200	1.024	0.24	0.03	8:1	Air	1.81×10^{-5}	293K
Apte and Yang[12]	2500	3.1	0.48	0.01	48:1	Air	1.66×10^{-5}	260K

TABLE II: Comparison of mode frequencies between the present linear stability analysis and the LES of Apte and Yang[12].

		Apte and Yang[12]	Present linear stability analysis	
		Physical frequency, f (Hz)	Physical frequency, f (Hz)	Dimensionless frequency, ω_r
$L/r=15$	P_1	1800	2060	83.46
	P_2	3500	3531	143.1
$L/r=24$	P_1	1800	–	–
	P_2	3600	3650	147.9

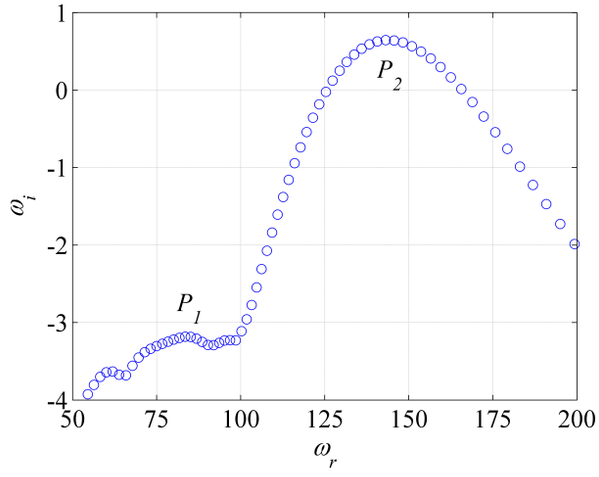

(a) $L/r=15$

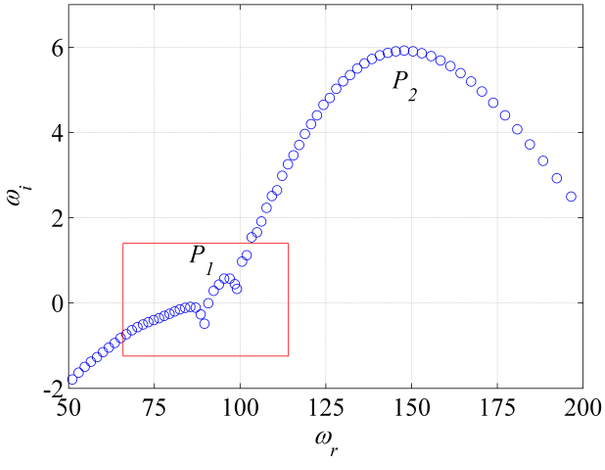

(b) $L/r=24$

FIG. 3: Eigenvalue spectra for Taylor–Culick flow at two representative values of the length-to-radius ratio(L/r):(a) $L/r=15$;(b) $L/r=24$.

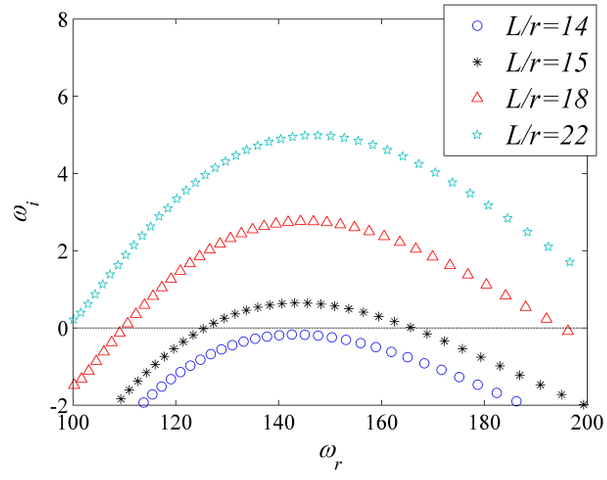

FIG. 4: Eigenvalue spectra for Taylor–Culick flow at $Re=2500$ and four different values of the length-to-radius ratio (L/r).

ratio (L/r). It can be seen that the initial base flow begins to lose stability at $14\leqslant L/r\leqslant 15$, where the local peak in ω_i on the eigenvalue branch first becomes positive.

The lateral-injection Reynolds number (Re) is also a key control parameter in the perturbation equations used for linear stability analysis[23]. With the length-to-radius ratio fixed at $L/r=13$, we show in Fig. 5a the influence of Re. It can be seen that the flow becomes more unstable as Re increases, with the critical value for instability occurring near $Re=5000$.

Application of the separation-of-variables technique to Eq. 4 enables the azimuthal perturbations to be characterized by m. When $m=0$, the perturbation variables are independent of the azimuthal coordinate. When m is real, the perturbation variables exhibit azimuthal periodicity. When m is complex, the perturbation variables exhibit spatial instability. In quasi-2D stability analysis, m is usually used as an input parameter. Flow instabilities in large-scale SRMs are governed predominately by their axial dynamics, so it is reasonable to assume that m is a real number for bi-global stability analysis

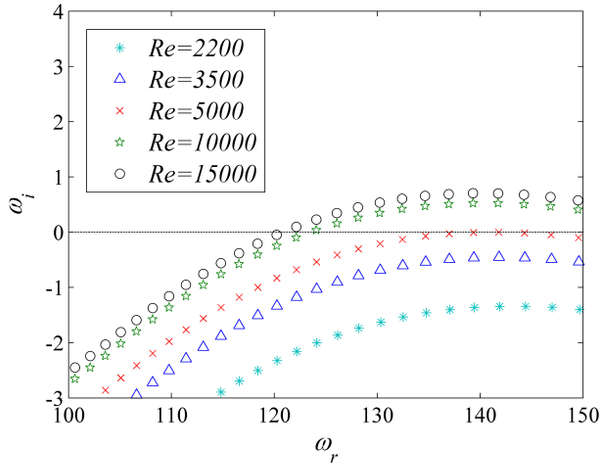

(a) Effect of Reynolds number at $L/r = 13$ and $m = 0$.

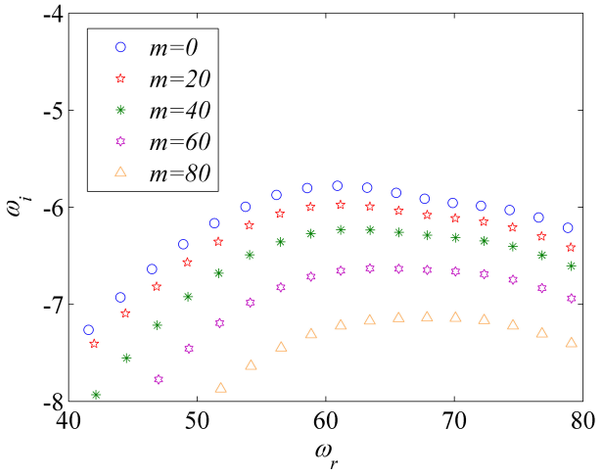

(b) Effect of m at $Re = 2200$ and $L/r = 8$.

FIG. 5: Eigenvalue spectra for Taylor–Culick flow at various conditions:(a) Eigen-spectra of different Reynolds numbers with fixed length to radius ratio and wave number;(b) Eigen-spectra of different wave numbers with fixed length to radius ratio and Reynolds number.

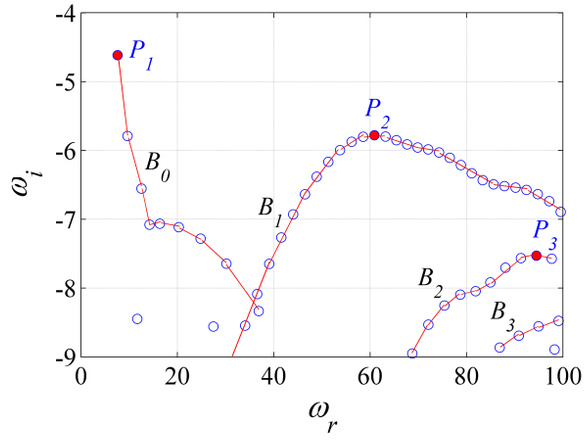

(a) Taylor–Culick flow

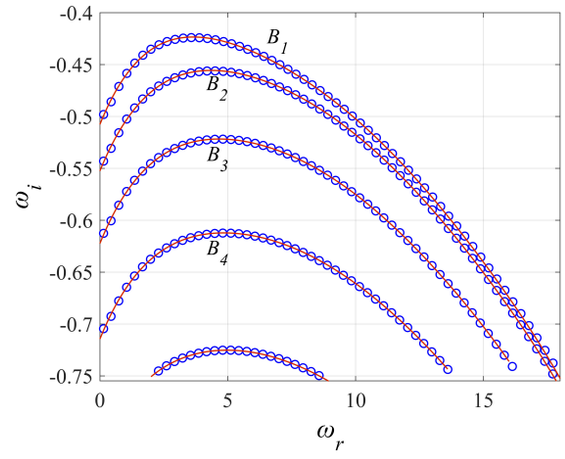

(b) Pipe flow

FIG. 6: Comparison of eigenvalue spectra at $Re = 2200$:(a) Eigen-branches of Taylor-Culick flow;(b) Eigen-branches of pipe flow.

in radial–axial coordinates. Fig. 5b shows the effect of m on the eigenvalue spectra. It can be seen that ω_i decreases with increasing m, implying that the $m = 0$ mode is the least stable. Consequently, for a conservative analysis, we focus on the $m = 0$ mode from here onwards.

B. Comparison with pipe flow

In cold flow, the Reynolds number is expected to be low. We therefore calculate the eigenvalue spectra for Taylor–Culick flow at $Re = 2200$ using grid dimensions of 30×250, as shown in Fig. 6a. For comparison, we perform a similar calculation for pipe flow with head injection at the same conditions, as shown in Fig. 6b. In both subfigures, the red lines represent the characteristic branches consisting of a family of eigenvalues (denoted by blue circular markers). The filled red markers are of particular interest. Labels B_0–B_n denote stable branches, while labels P_1–P_3 denote eigenvalues of interest.

An examination of the eigenvalue spectra in Fig. 6 shows that both Taylor–Culick flow and pipe flow are stable, with ω_i taking on negative values for all branches considered here. The eigenvalue spectrum for pipe flow contains characteristic branches whose attenuation rate increases successively from B_1 to B_n (Fig. 6b). Each of these branches consists of a large number of discrete eigenvalues, which represent the intrinsic frequencies of the perturbations and which correspond to different spatial perturbation patterns, as will be shown in Fig. 8. It should be noted that the discreteness of the eigenvalues is independent of the numerical method used. Coupling reso-

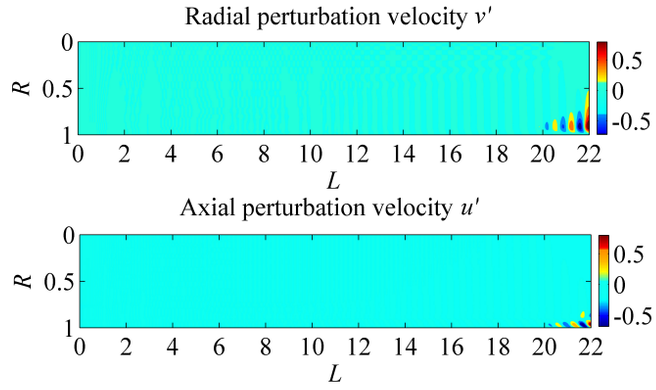

FIG. 7: Results from our linear stability analysis.

nance may occur if an external excitation source is present at an appropriate frequency close to that of an eigenvalue. For each branch, the largest value of ω_i is of particular interest, as the corresponding spatial perturbation pattern is the one that is most easily excited and hence most readily observable in an actual nonlinear flow.

The eigenvalue spectra for Taylor–Culick flow contain branch structures B_0–B_n, as shown in Fig. 6a. The main difference with respect to pipe flow (Fig. 6b) is in the B_0 branch, which appears only in Taylor–Culick flow. As for the other branches, the instability frequencies for Taylor–Culick flow are consistently higher than those for pipe flow. Furthermore, ω_i for Taylor–Culick flow is an order of magnitude smaller than that for pipe flow, indicating greater stability. In the next section, we provide a more detailed analysis of the associated eigenvectors.

V. PERTURBATION CHARACTERISTICS

A. Spatial distribution of perturbation components

By examining the growth rate alongside the spatial perturbation pattern, one can gain further insight into the characteristics of the unstable modes. The spatial form of such modes can be extracted via CFD by subtracting the time-averaged flow field from the instantaneous flow field. For example, we consider LES of the flow in a lateral injection channel by Apte and Yang[12]. The results of Apte and this article can be used as mutual verification. As the flow evolves downstream, the perturbation variables can be seen growing progressively. Our linear stability analysis (Fig. 7) produces an accurate estimate of the velocity fluctuations upstream of the transition zone. This suggests that the transition dynamics is potentially governed by the linear mechanisms near the inception of instability.

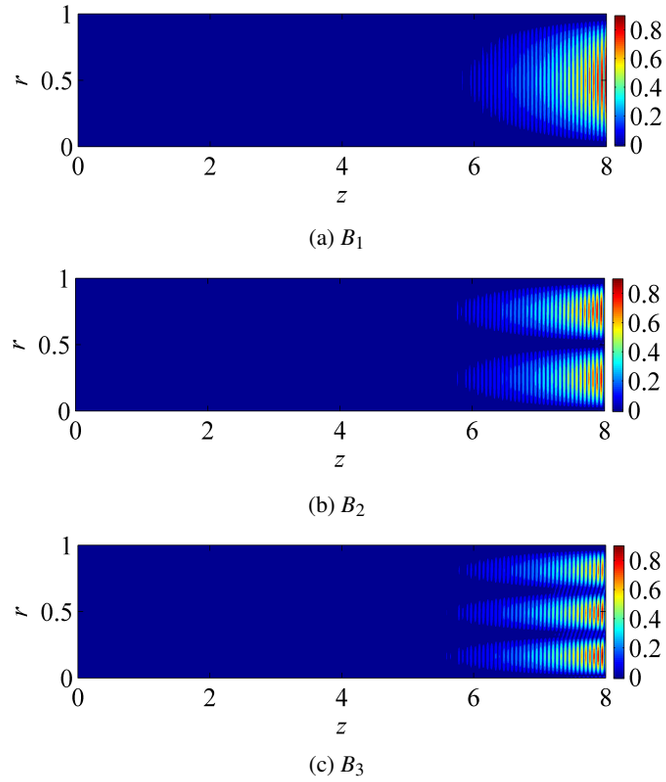

(a) B_1

(b) B_2

(c) B_3

FIG. 8: Velocity perturbation amplitude in pipe flow:(a) Eigenvector in branch B_1;(b) Eigenvector in branch B_2; and (c) Eigenvector in branch B_3 .

B. Comparison of bi-global modes: Taylor–Culick flow vs pipe flow

Fig. 8 shows the spatial distribution of the velocity perturbation amplitude for branches B_1, B_2 and B_3 in pipe flow (see Fig. 6b for reference). It can be seen that the perturbation distribution is fairly weak and uniform throughout the initial part of the flow domain ($z < 6$), but it then develops high-amplitude radially periodic structures at the downstream end ($6 < z < 8$), resulting in peak values at a station of $z = 8$.

As for Taylor–Culick flow, we show in Fig. 9 the spatial distribution of the velocity perturbation amplitude for eigenvalues P_1, P_2 and P_3 from Fig. 6a. For eigenvalue P_1, which sits on a branch (B_0) that does not exist in pipe flow, the perturbation distribution is concentrated at the central axis (Fig. 9a). This is due to the radially symmetric velocity injection: flow is first injected with its momentum perpendicular to the wall surface but is then redirected in a direction parallel to the central axis. The perturbation distribution for eigenvalues P_2 (Fig. 9b) and P_3 (Fig. 9c) show that, unlike pipe flow (Fig. 8), Taylor–Culick flow does not exhibit radially periodic structures. Instead axially periodic structures emerge in the outer-half of the chamber radius, with the structures for eigenvalue P_3 extending farther upstream than those for eigenvalue P_2.

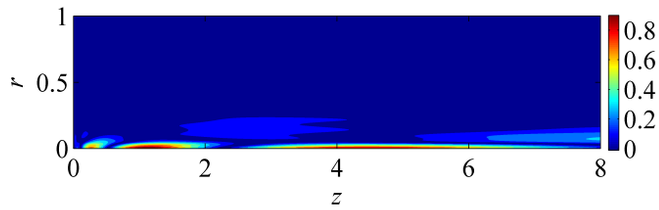

(a) P_1

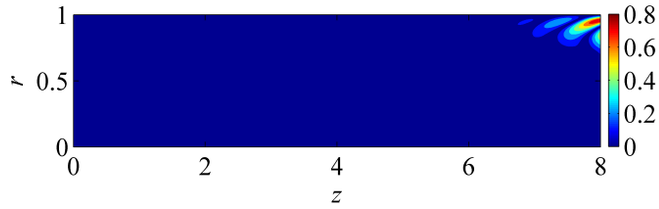

(b) P_2

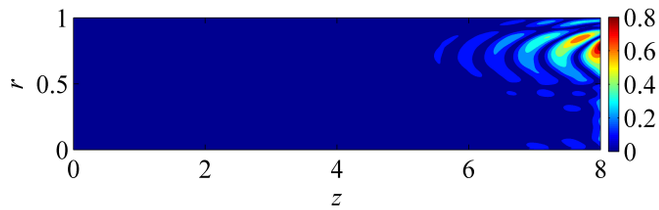

(c) P_3

FIG. 9: Velocity perturbation amplitude in Taylor–Culick flow:(a) Eigenvalue of P_1; (b) Eigenvalue of P_2; and (c) Eigenvalue of P_3.

C. Instability mechanism

1. *Effect of amphidromic points*

In Table II, we showed that the frequency of mode P_2 is in close agreement with that predicted by the LES of Apte and Yang[12]. We therefore focus on this particular mode in the following analysis. Fig. 10 shows contours of the velocity perturbation amplitude for mode P_2 in Taylor–Culick flow. The black dotted lines are the mean flow streamlines, the rainbow solid lines are contours of the velocity perturbation amplitude, and the green/red boxes highlight the local maxima and minima. All of these instability features are consistent with those identified in previous research[16].

An examination of the mean flow streamlines in Fig. 10 reveals evidence of flow turning, which arises from a series of extreme points in the velocity perturbation distribution; such points are absent in pipe flow. The maximum points, which are located between the minimum points and the wall, exhibit spatial periodicity in the axial z direction. As mentioned earlier, the perturbation distribution for Taylor–Culick flow (Fig. 9b) is concentrated near the wall surface at the downstream end of the chamber, at around $7 < z < 8$. By contrast, the perturbation distribution for pipe flow (Fig. 8b) is distributed more evenly in the radial direction and extends farther upstream to around $z = 6$. The mean flow streamlines have substantial components in the z direction after the minimum points, indicating that the flow has already turned significantly even before reaching the central axis itself. We note that the minimum points sit in the upstream region along the mean flow streamlines and that the radial velocity decreases downstream. This has the effect of reducing the local Reynolds number and turbulence level after the minimum points, giving rise to a more stable internal region. Consequently, the flow on either side of the minimum points exhibits different properties, leading to the formation of an S-shaped contour in the perturbation distribution (Fig. 10). Such minimum points are often referred to as amphidromic points[16].

The relationship between flow turning and amphidromic points can be seen more clearly in the velocity profile. Fig. 11a and Fig. 12a show the axial growth curves for velocity perturbations in Taylor–Culick flow and in pipe flow, respectively. In pipe flow (Fig. 12a), the perturbations can be seen growing exponentially in the axial z direction. In Taylor–Culick flow (Fig. 11a), however, the existence of amphidromic points interrupts the exponential growth at a certain radial distance from the wall surface, but the perturbation evolution outside this region remains largely unaffected. This illustrates the influence of amphidromic points on flow turning.

Figure. 11b and 12b show the radial growth curves for velocity perturbations in Taylor–Culick flow and in pipe flow, respectively. In pipe flow (Fig. 12b), the perturbations contaminate the entire domain, forming clear patterns of radial periodicity that extend from the wall surface (outer region) to the central axis (inner region). In Taylor–Culick flow (Fig. 11b), however, the existence of amphidromic points divides the local flow field into two distinct regions, an outer region with strong perturbations and an inner region with weak perturbations. This shows that the existence of amphidromic points limits the inward radial expansion of perturbations.

An inspection of the velocity perturbation streamlines, shown in Fig. 13, provides further insight into how the amphidromic points can weaken the perturbations near the central axis at the downstream end of the chamber. It can be seen that the velocity perturbation streamlines do not develop internally, as if there were a boundary impeding the propagation of perturbations. Furthermore, as the flow velocity increases, the amphidromic points divide the flow field into two regions: an outer region where surface disturbances arise, and an inner region where the streamlines resemble those of pipe flow. This indicates that a boundary layer of perturbations is generated as a disturbance source.

2. *Vortex generation*

It is clear that flow turning impairs the propagation of perturbations at the downstream end of the chamber. Next we examine the velocity perturbation vectors in order to better understand how this mechanism can generate vortices in an actual flow. Fig. 14 shows the detailed structure of the velocity perturbation vectors. Patterns of strong periodic advection can be observed. Although the local advection of velocity perturbations cannot generate vortices directly, such disturbances

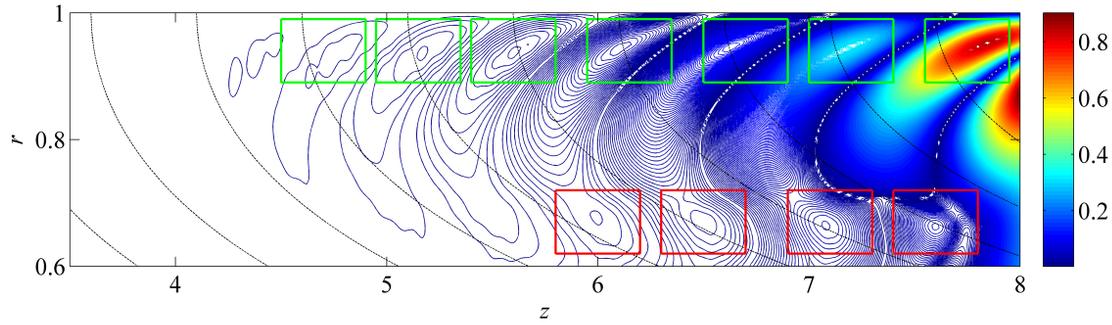

FIG. 10: Contours of the velocity perturbation amplitude for mode P_2 in Taylor–Culick flow.

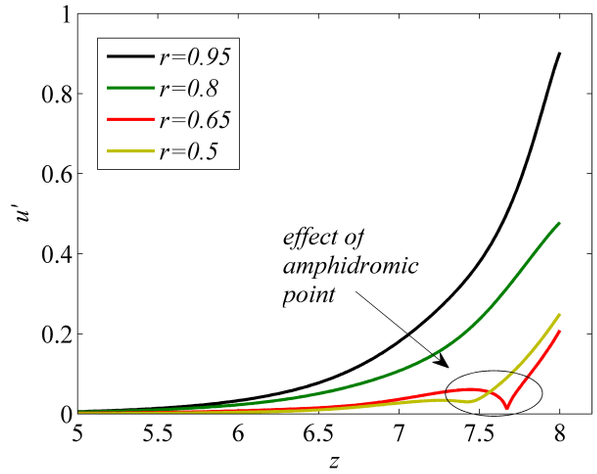

(a) Axial growth curve

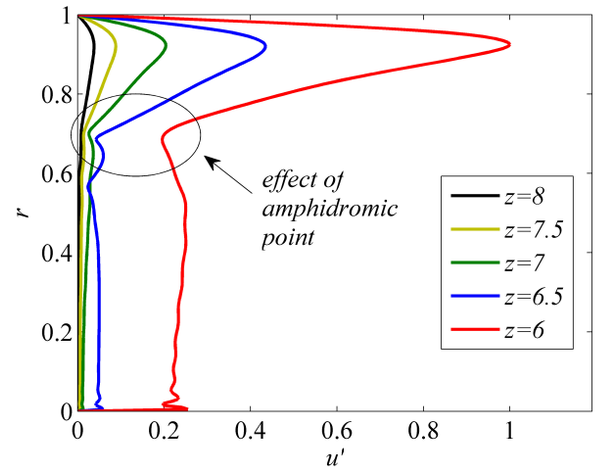

(b) Radial growth curve

FIG. 11: Growth curve of velocity perturbations in Taylor–Culick flow:(a) Axial growth curve;(b) Radial growth curve.

can accumulate in the flow field and change the mean flow. When combined with the exponential growth of perturbations in the axial z direction, this phenomenon can enhance local velocity differences near the wall, particularly at the downstream end of the chamber, contributing to increased shear.

Another possible cause of vortices is a change in pressure. Fig. 15 compares the spatial distribution of pressure perturbations in Taylor–Culick flow and pipe flow. Fig. 16 shows the axial and radial growth curves for pressure perturbations in Taylor–Culick flow, while Fig. 17 shows analogous curves for pipe flow. Far downstream ($6 < z < 8$), the pressure perturbation distribution in Taylor–Culick flow (Fig. 15a) shares certain features with that in pipe flow (Fig. 15b), such as patterns of axial periodicity that grow in amplitude as the downstream distance z increases. However, unlike that in pipe flow, the pressure perturbation distribution in Taylor–Culick flow shows little evidence of periodic structures in the radial direction. Because the radial velocity in pipe flow is zero, the perturbations can propagate freely, producing high-order harmonic frequencies associated with symmetric modes. In Fig. 8, a similar phenomenon was observed in the velocity perturbation distribution.

As mentioned earlier, the radial velocity in Taylor–Culick flow decreases rapidly, with amphidromic points dividing the flow into two distinct regions. In particular, strong perturbations are restricted to the near-wall region, and changes in the pressure mode arise between the amphidromic points and the wall itself, as shown in Fig. 16b and Fig. 17b. Fig. 16a shows the pressure perturbations at different radial locations. Close to the wall ($r = 0.6, 0.68, 0.84$), the pressure perturbations vary significantly, much like the velocity perturbations do (Fig. 11b), whereas those near the central axis ($r = 0.1, 0.2, 0.3$) vary to a much lower degree. Fig. 16b captures the effect of the amphidromic points on the pressure perturbations. The gradient in the pressure perturbations undergoes a marked change on both sides of the amphidromic points, which sit at around $r = 0.6$. The shear stresses generated by the pressure difference between the two sides of the amphidromic points strengthen the advection of velocity perturbations during flow development.

Figure. 18 shows the relationship between pressure and velocity perturbations in Taylor–Culick flow. The pressure per-

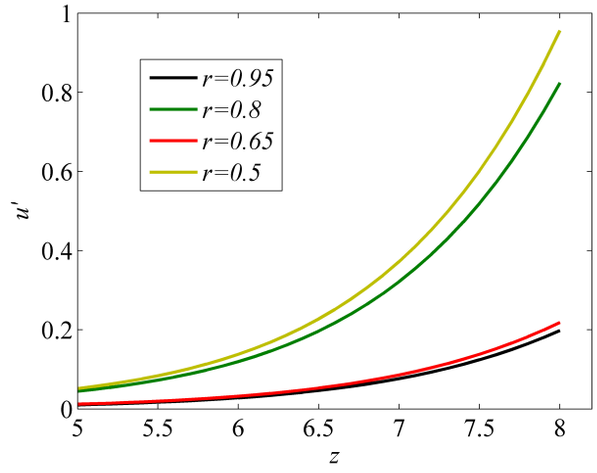

(a) Axial growth curve

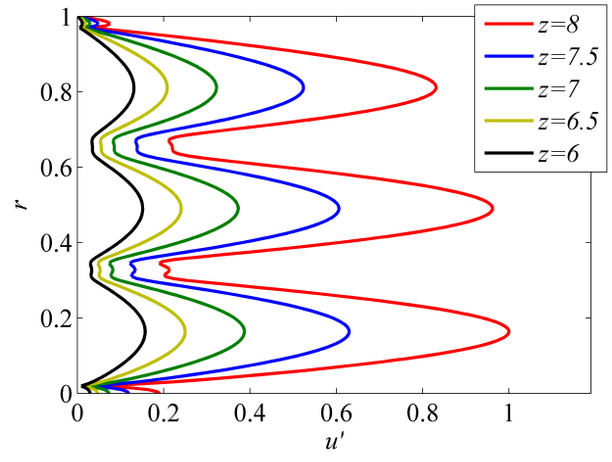

(b) Radial growth curve

FIG. 12: Growth curve of velocity perturbations in pipe flow:(a) Axial growth curve;(b) Radial growth curve.

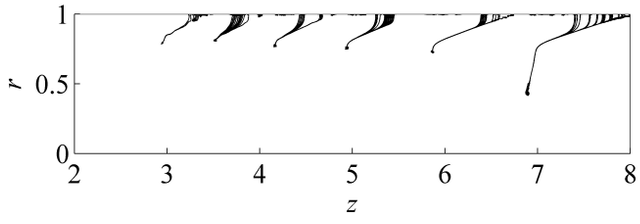

FIG. 13: Velocity perturbation streamlines for mode P_2 in Taylor–Culick flow.

turbations are represented by contours, while the velocity perturbations are represented by vectors. Fig. 18a and Fig. 18c show the flow fields near two local pressure minima, while Fig. 18b shows the flow field near a local pressure maximum between the two pressure minima. In both Fig. 18a and Fig. 18c, a pronounced back-flow feature can be identified. Moreover, the pressure and velocity perturbations exhibit synchronized periodicity, providing direct evidence of parietal vortex shedding.

An overall negative pressure perturbation field is observed in Taylor–Culick flow (Fig. 16), but only minor fluctuations about the equilibrium pressure are observed in pipe flow (Fig. 17). Furthermore, Fig. 17a shows the emergence of pressure oscillations at the downstream end of pipe flow. This suggests that the perturbations in Taylor–Culick flow produce stronger feedback effects on the flow field than those in pipe flow. To explore this, we show in Fig. 19 the spatial distribution of vorticity perturbations for mode P_2 in Taylor–Culick flow. It can be seen that the vorticity perturbations fluctuate along the flow streamlines, reaching a maximum near the wall at the downstream end of the chamber.

From the discussion above, it is clear that the existence of amphidromic points in Taylor–Culick flow can cause parietal vortex shedding in the following way. First, the amphidromic points confine the downstream flow perturbations to the near-wall region. Then, the velocity perturbations near the wall develop periodic advection patterns. Meanwhile, the shear stresses generated by the pressure difference between the two sides of the amphidromic points facilitate the formation of vortices. This explains how vortices can be generated by flow turning in Taylor–Culick flow.

VI. CONCLUSIONS

In this theoretical study, we have used linear stability analysis to explore a mechanism for parietal vortex shedding in Taylor–Culick flow, which is representative of the flow in SRMs. We used previously published LES data to validate theoretical predictions of the dominant eigenvalues. We found that flow turning, which arises from lateral mass injection, plays a key role in the formation of parietal vortex shedding. We also found that the amphidromic points, which arise from flow-turning effects, can divide the flow field into two distinct regions, an outer region with strong perturbations and an inner region with weak perturbations. In the outer region, the velocity perturbations were found to develop advection patterns with axial (streamwise) periodicity. Furthermore, the pressure perturbations were found to induce flow gradients that increased shear stresses. Together these effects combine to form a mechanism for the generation of parietal vortex shedding in SRM chambers.

ACKNOWLEDGMENTS

This work was funded by the China Postdoctoral Science Foundation(Grant No.2019M653751)

DATA AVAILABILITY

The data that support the findings of this study are available from the corresponding author upon reasonable request.

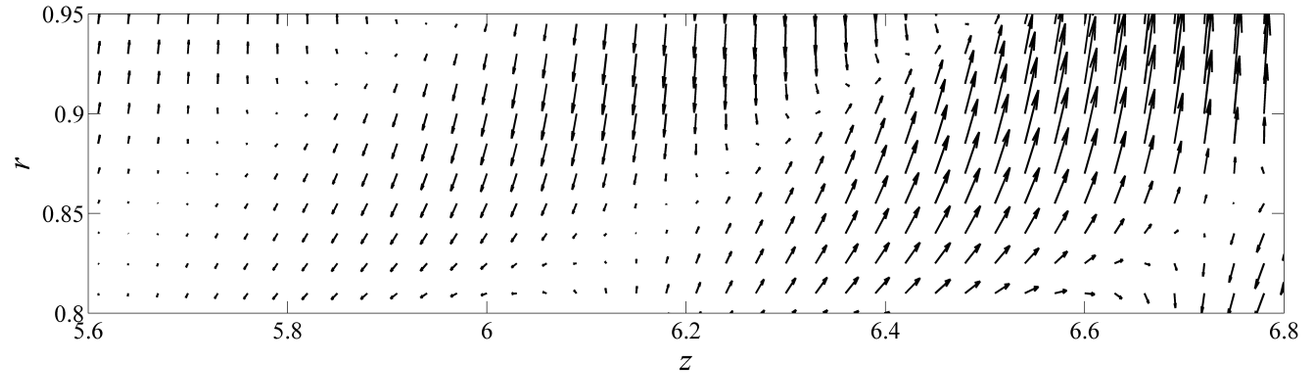

FIG. 14: Velocity perturbation vectors for mode P_2 in Taylor–Culick flow.

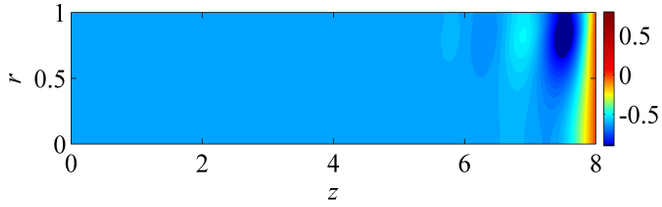

(a) Eigenvector of P_2 in Taylor–Culick flow

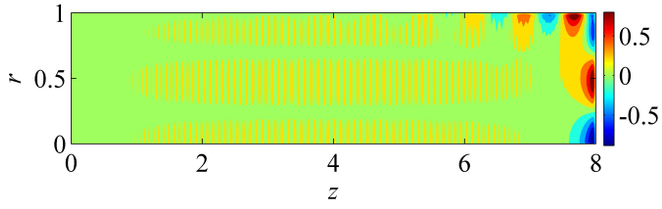

(b) Eigenvector of Branch B_1 in pipe flow

FIG. 15: Spatial distribution of pressure perturbations:(a) Eigenvector of P_2 in Taylor–Culick flow;(b) Eigenvector of Branch B_1 in pipe flow.

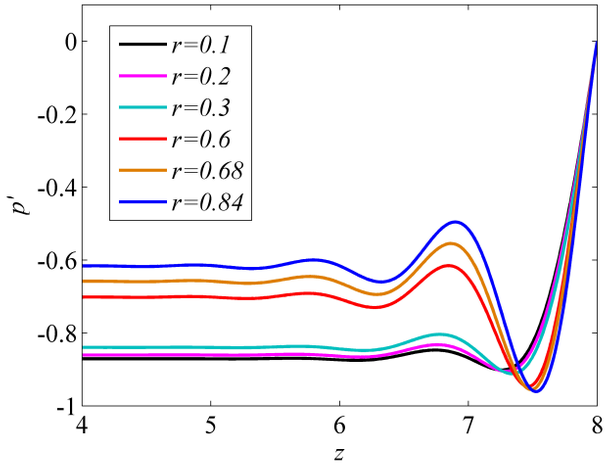

(a) Axial growth curve

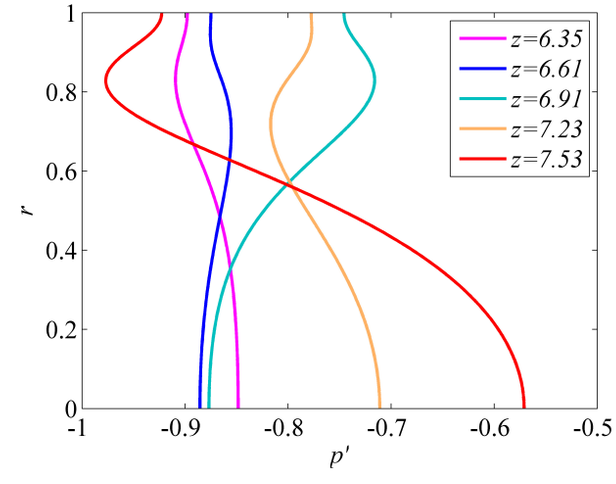

(b) Radial growth curve

FIG. 16: Growth curve of pressure perturbations in Taylor–Culick flow:(a) Axial growth curve;(b) Radial growth curve.

[1]G. A. Flandro, "Vortex driving mechanisms in oscillatory rocket flows," Journal of Propulsion and Power **2**, 206–214 (1986).
[2]K. W. Dotson, S. Koshigoe, and K. K. Pace, "Vortex shedding in a large solid rocket motor without inhibitors at the segment interfaces," Journal of Propulsion and Power **13**, 197–206 (1997).
[3]F. Blomshield, "Historical perspective of combustion instability in motors – case studies," in *37th Joint Propulsion Conference and Exhibit* (American Institute of Aeronautics and Astronautics, 2001).
[4]Y. Fabignon, J. Dupays, G. Avalon, F. Vuillot, N. Lupoglazoff, G. Casalis, and et al., "Instabilities and pressure oscillations in solid rocket motors," Aerospace Science and Technology **7**, 191–200 (2003).
[5]N. Lupoglazoff and F. Vuillot, "Numerical simulations of parietal vortex-shedding phenomenon in a cold flow set-up," in *34th AIAA/ASME/SAE/ASEE Joint Propulsion Conference and Exhibit* (American Institute of Aeronautics and Astronautics, 1998).
[6]G. Avalon, B. Ugurtas, F. Grisch, and A. Bresson, "Numerical computations and visualization tests of the flow inside a cold gas simulation with characterization of a parietal vortex shedding," in *AIAA/ASME/SAE/ASEE Joint Propulsion Conference and Exhibit* (American Institute of Aeronautics and Astronautics, 2013).
[7]G. Avalon and D. Lambert, "Cold gas experiments applied to the understanding of aeroacoustic phenomena inside solid propellant boosters,"

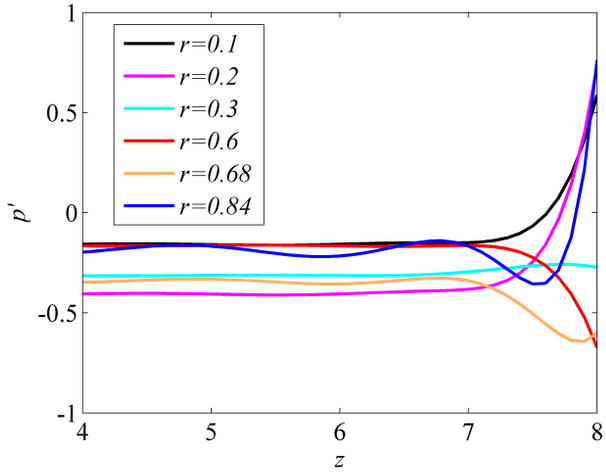

(a) Axial growth curve

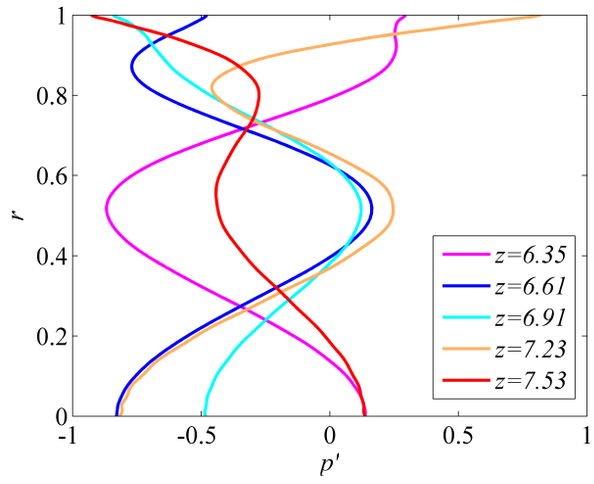

(b) Radial growth curve

FIG. 17: Growth curve of pressure perturbations in pipe flow:(a) Axial growth curve;(b) Radial growth curve.

in *42nd AIAA/ASME/SAE/ASEE Joint Propulsion Conference and Exhibit* (American Institute of Aeronautics and Astronautics, 2006).

[8]G. Casalis, G. Avalon, and J. P. Pineau, "Spatial instability of planar channel flow with fluid injection through porous walls," Phys. Fluids **10**, 2558—-2568 (1998).

[9]J. Griffond and G. Casalis, "On the dependence on the formulation of some nonparallel stability approaches applied to the Taylor flow," Phys. Fluids **12**, 466—-468 (2000).

[10]F. Chedevergne, G. Casalis, and T. Feraille, "Biglobal linear stability analysis of the flow induced by wall injection," Phys. Fluids **18**, 014103 (2006).

[11]N. Lupoglazoff and F. Vuillot, "Parietal vortex shedding as a cause of instability for long solid propellant motors - numerial simulations and comparisons with firing tests," in *Aerospace Sciences Meeting and Exhibit* (American Institute of Aeronautics and Astronautics, 1996).

[12]S. Apte and V. Yang, "Unsteady flow evolution in porous chamber with surface mass injection, part 1: free oscillation," AIAA Journal **39**, 1577–1586 (2001).

[13]T. Y. Qi, C. Liu, M. J. Ni, and J. C. Yang, "The linear stability of Hunt-Rayleigh-Bénard flow," Phys. Fluids **29**, 064103 (2017).

[14]A. Kourta, "Instability of channel flow with fluid injection and parietal vortex shedding," Computers & Fluids **33**, 155–178 (2004).

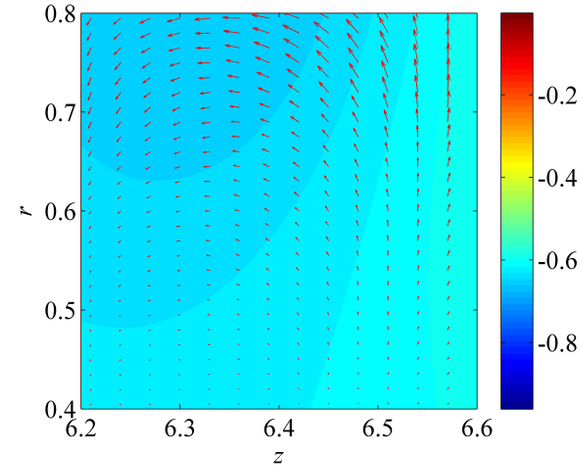

(a)

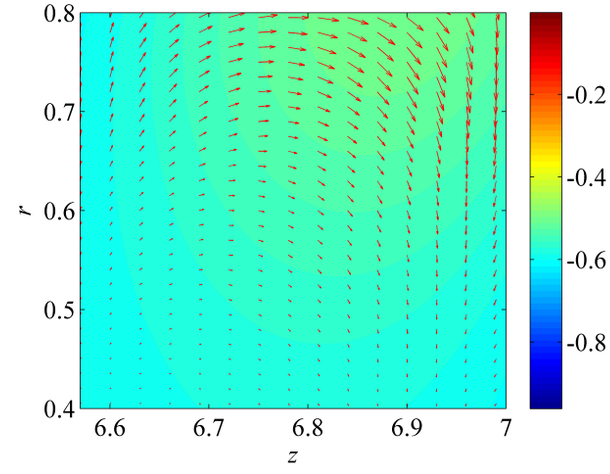

(b)

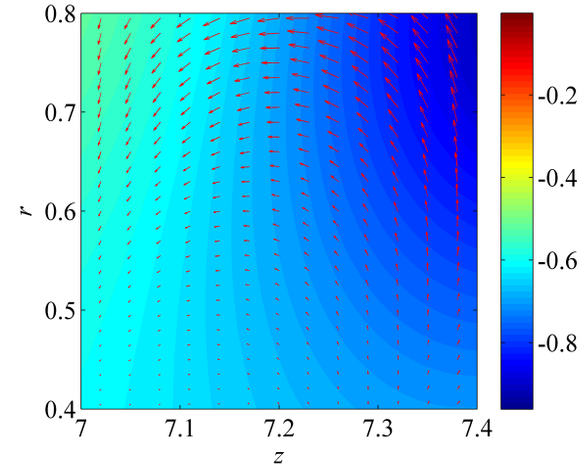

(c)

FIG. 18: Velocity perturbations (vectors) superimposed over pressure perturbations (contours) in Taylor–Culick flow:(a) $6.2 < z < 6.6$; (b) $6.6 < z < 7$; and (c) $7 < z < 7.4$.

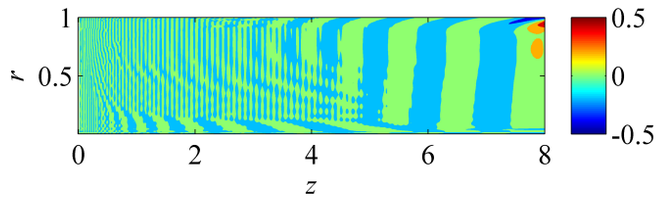

FIG. 19: Vorticity perturbations for mode P_2 in Taylor–Culick flow.

[15]G. Boyer, G. Casalis, and J. L. Estivalèzes, "Stability analysis and numerical simulation of simplified solid rocket motors," Phys. Fluids **25**, 084109 (2013).
[16]G. Boyer, G. Casalis, and J. Estivalèzes, "Theoretical investigation of the parietal vortex shedding in solid rocket motors," in *8th AIAA/ASME/SAE/ASEE Joint Propulsion Conference & Exhibit* (American Institute of Aeronautics and Astronautics, 2012).
[17]Y. Guan, P. Liu, B. Jin, V. Gupta, and L. K. Li, "Nonlinear time-series analysis of thermoacoustic oscillations in a solid rocket motor," Experimental Thermal and Fluid Science **98**, 217–226 (2018).
[18]W. Ao, Z. Fan, L. Liu, Y. An, J. Ren, M. Zhao, P. Liu, and L. K. Li, "Agglomeration and combustion characteristics of solid composite propellants containing aluminum-based alloys," Combustion and Flame **220**, 288–297 (2020).
[19]W. Ao, P. Liu, H. Liu, S. Wu, B. Tao, X. Huang, and L. K. Li, "Tuning the agglomeration and combustion characteristics of aluminized propellants via a new functionalized fluoropolymer," Chemical Engineering Journal **382**, 122987 (2020).
[20]P. Liu, M. Wang, W. Yang, V. Gupta, Y. Guan, and L. K. Li, "Modified computation of the nozzle damping coefficient in solid rocket motors," Acta Astronautica **143**, 391–397 (2018).
[21]Y. Li, Z. Wang, and P. Liu, "On the grid dependence of hydrodynamic stability analysis in solid rocket motors," Phys. Fluids **32**, 034103 (2020).
[22]V. Theofilis, "Global linear instability," Annual Review of Fluid Mechanics **43**, 319–352 (2011).
[23]D. Couton, F. Plourde, and S. Doan-Kim, "Cold gas simulation of a solid propellant rocket motor," AIAA Journal **34**, 2514–2522 (1996).
[24]J. A. C. Weideman and S. C. Reddy, "A matlab differentiation matrix suite," ACM Transactions on Mathematical Software **26**, 465–519 (2000).
[25]E. Beutler, "Spectral methods in matlab," (SIAM, Philadelphia, 2000).

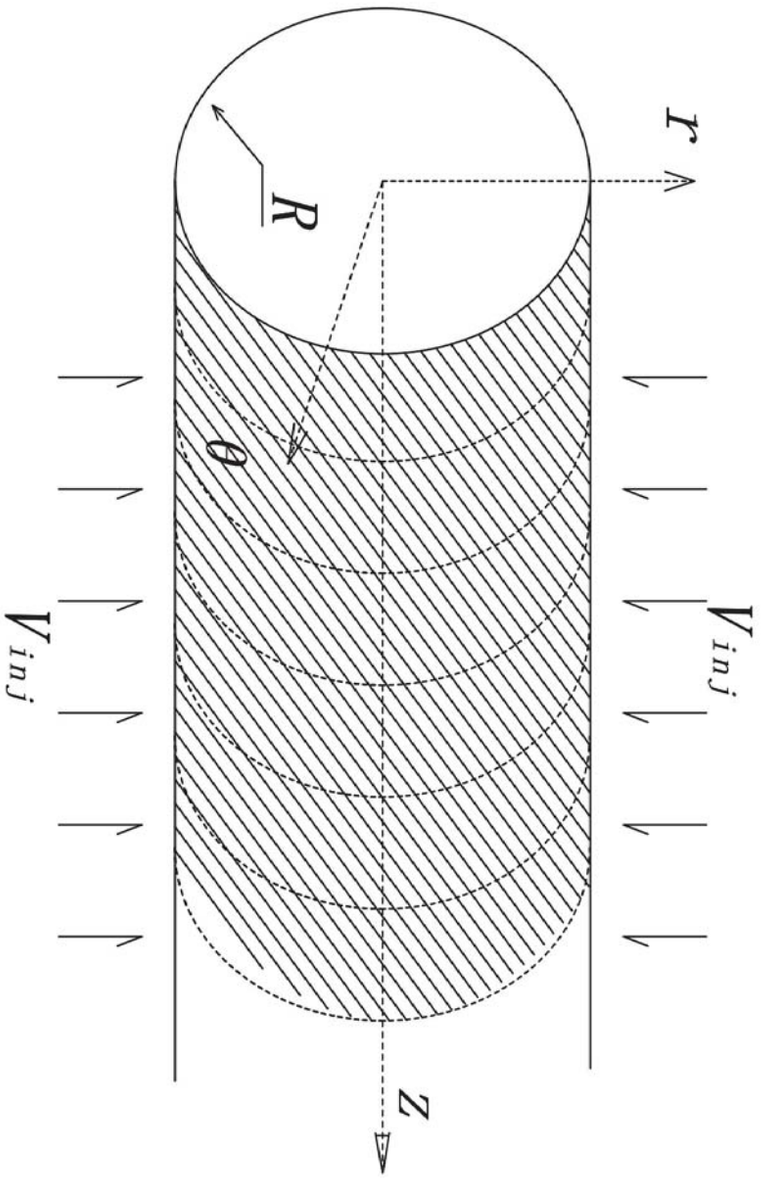

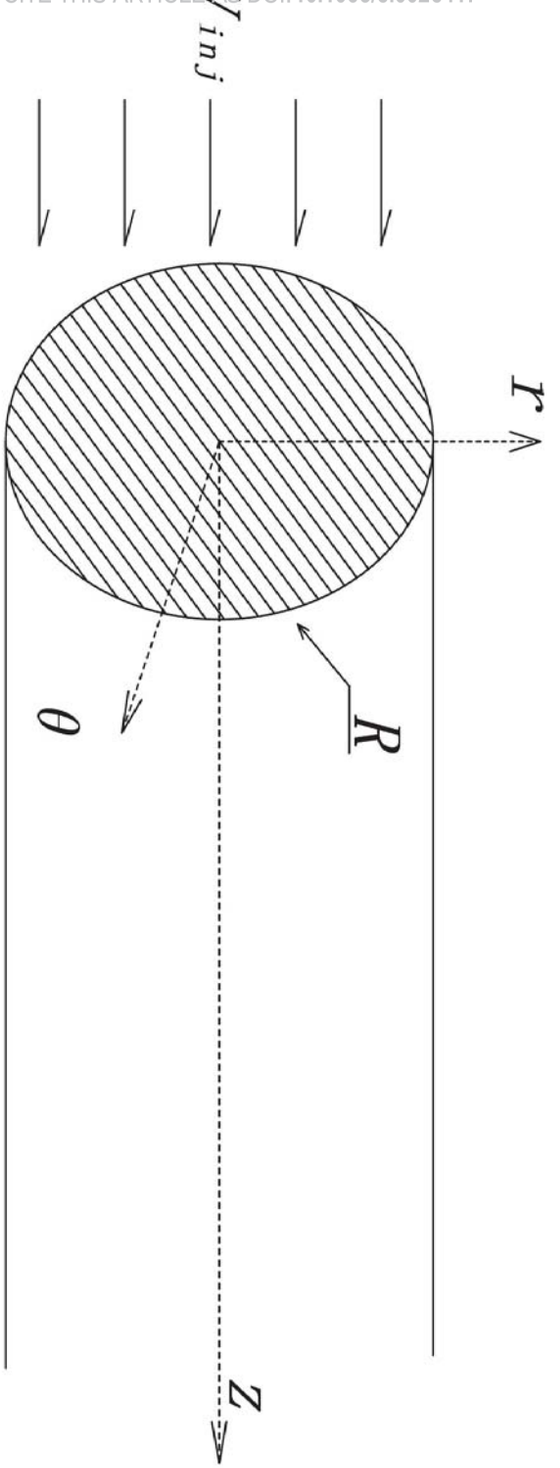

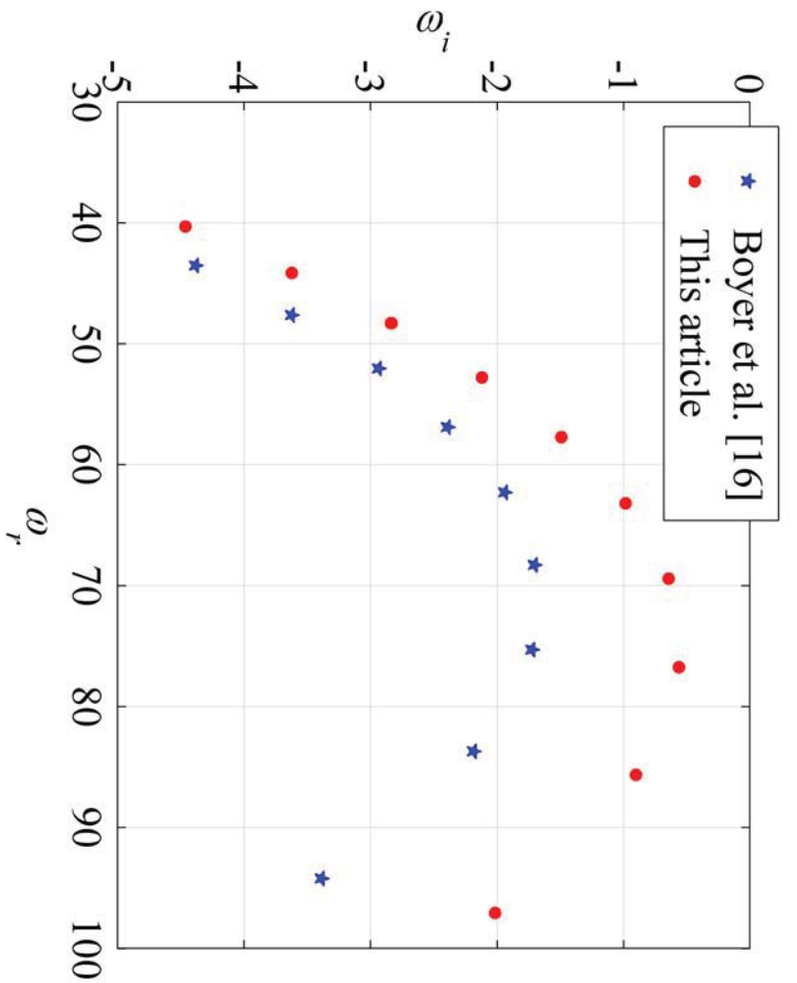

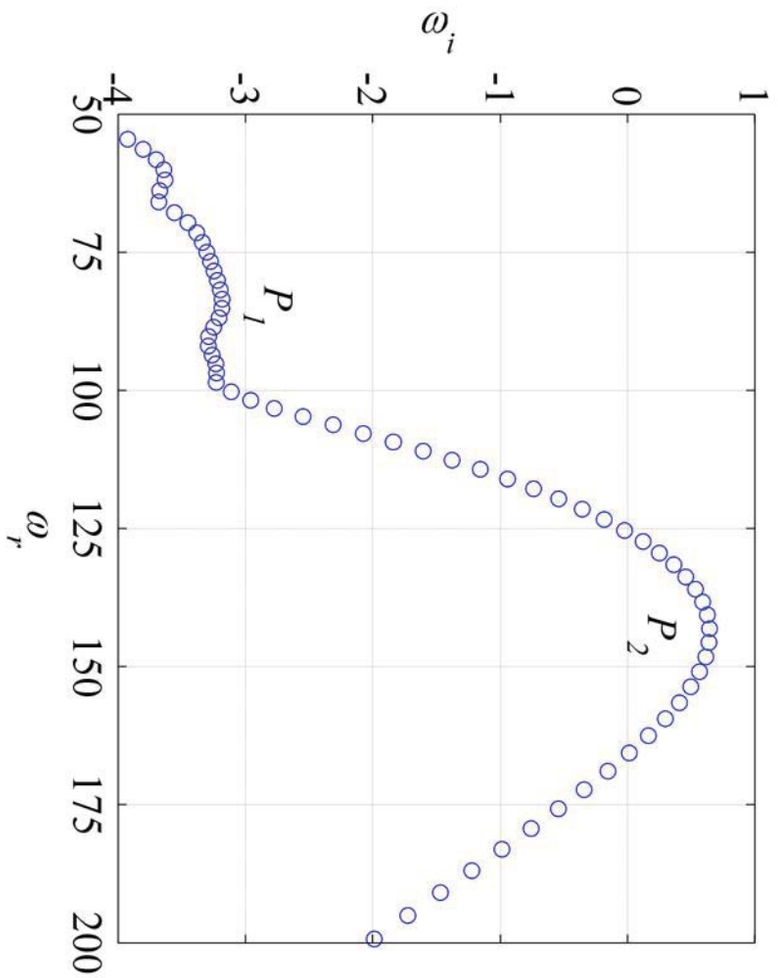

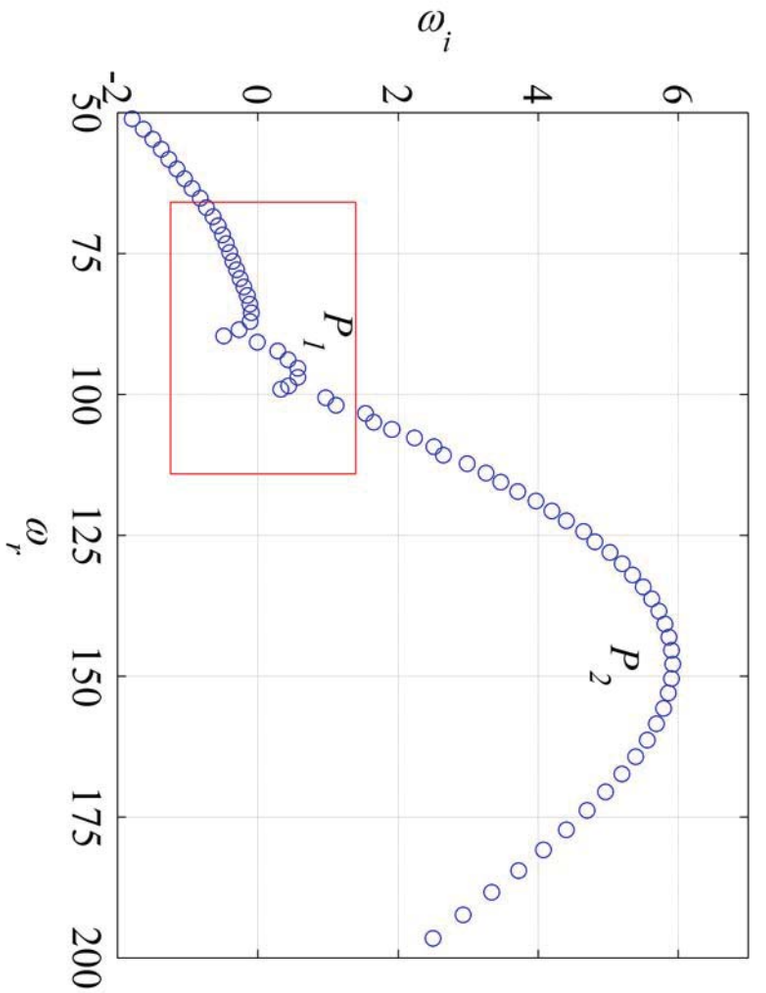

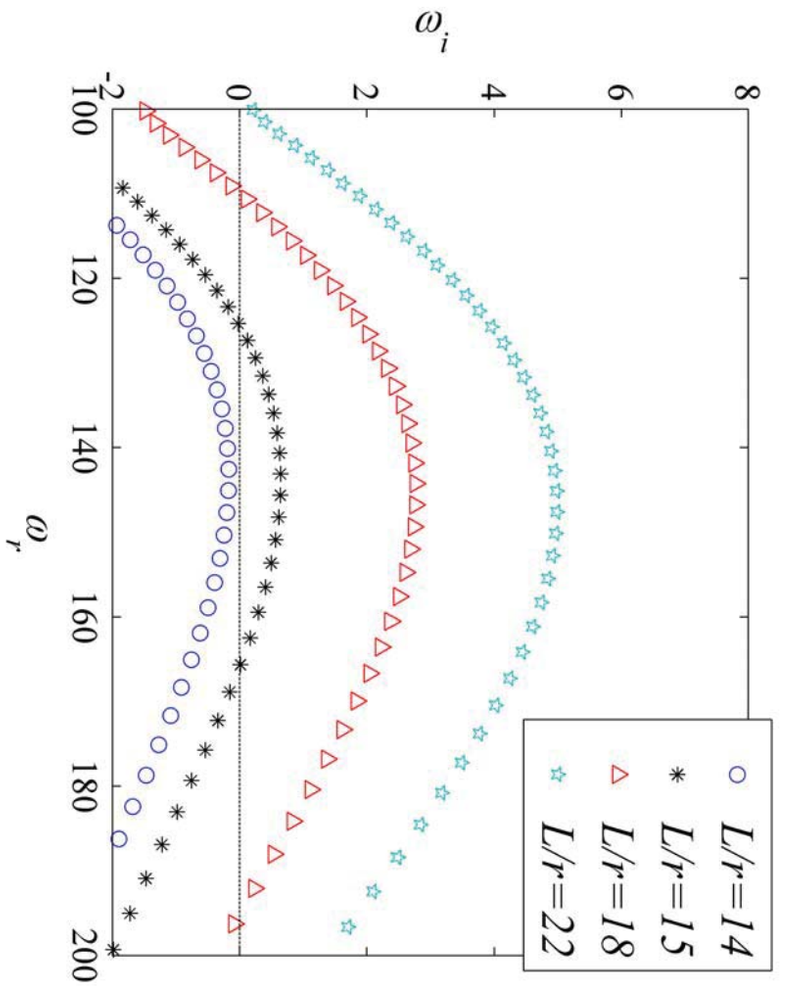

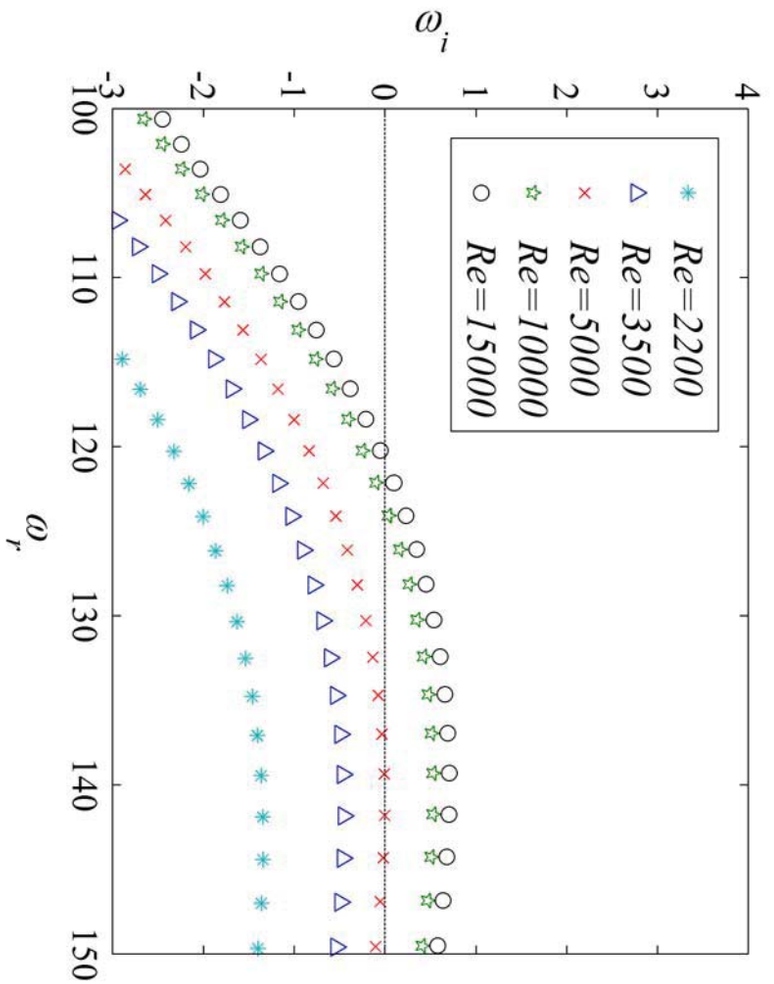

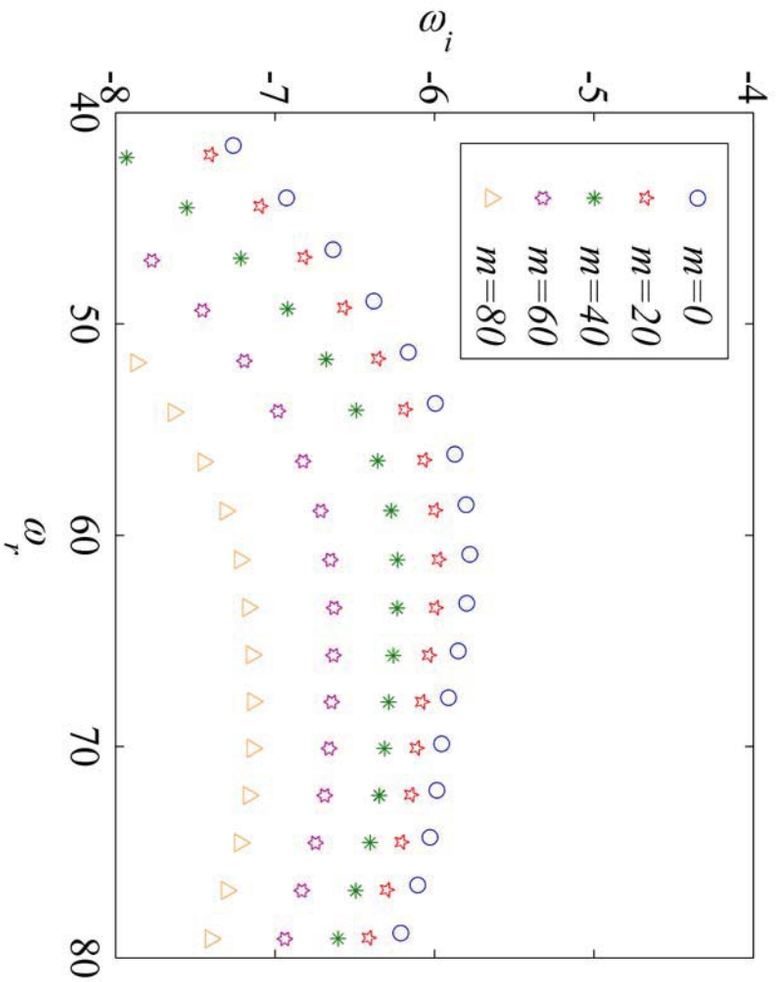

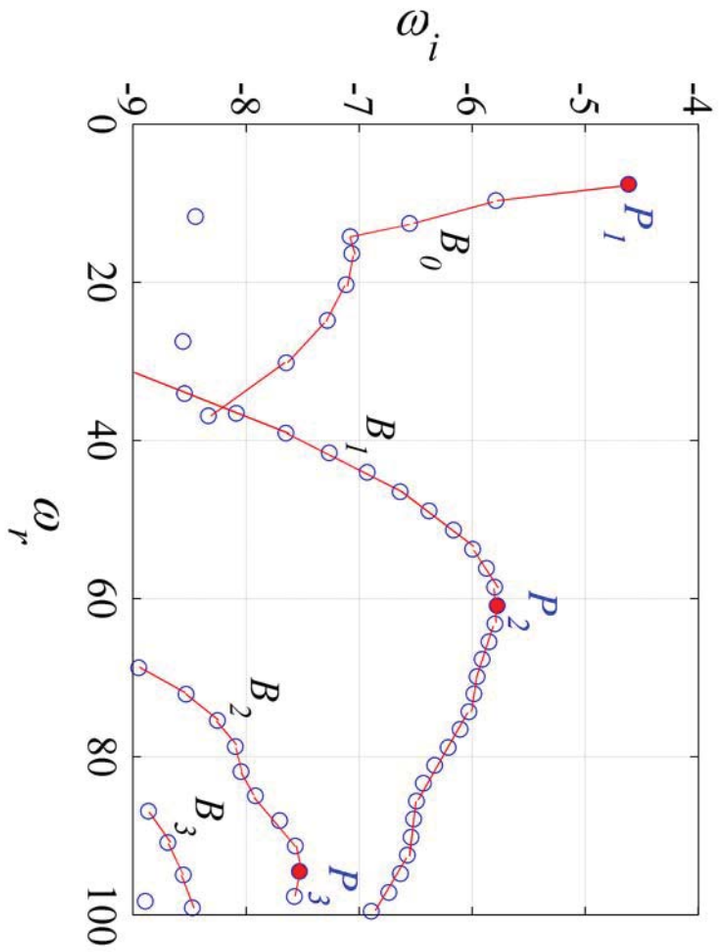

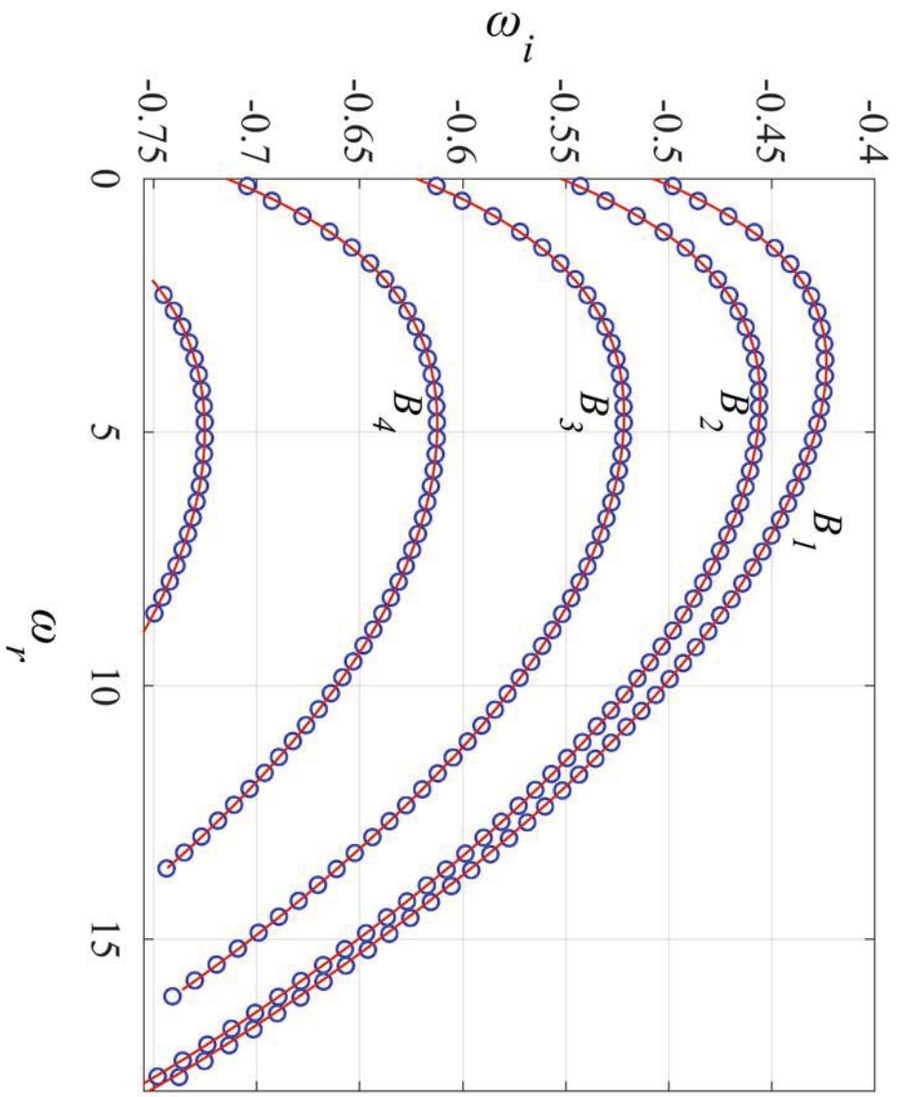

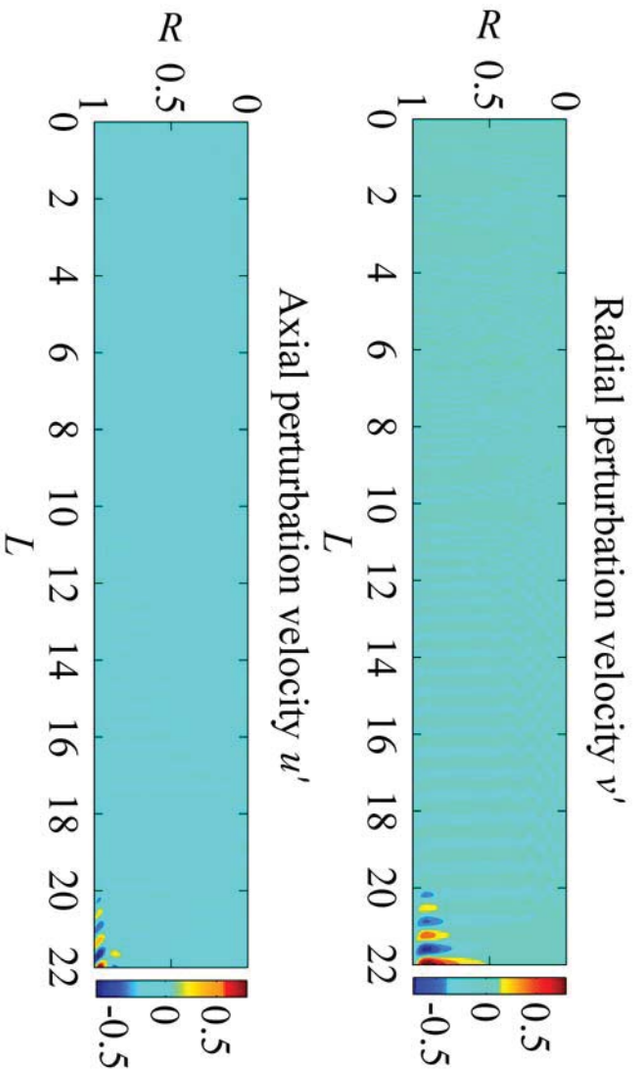

PLEASE CITE THIS ARTICLE AS DOI: 10.1063/5.0025417

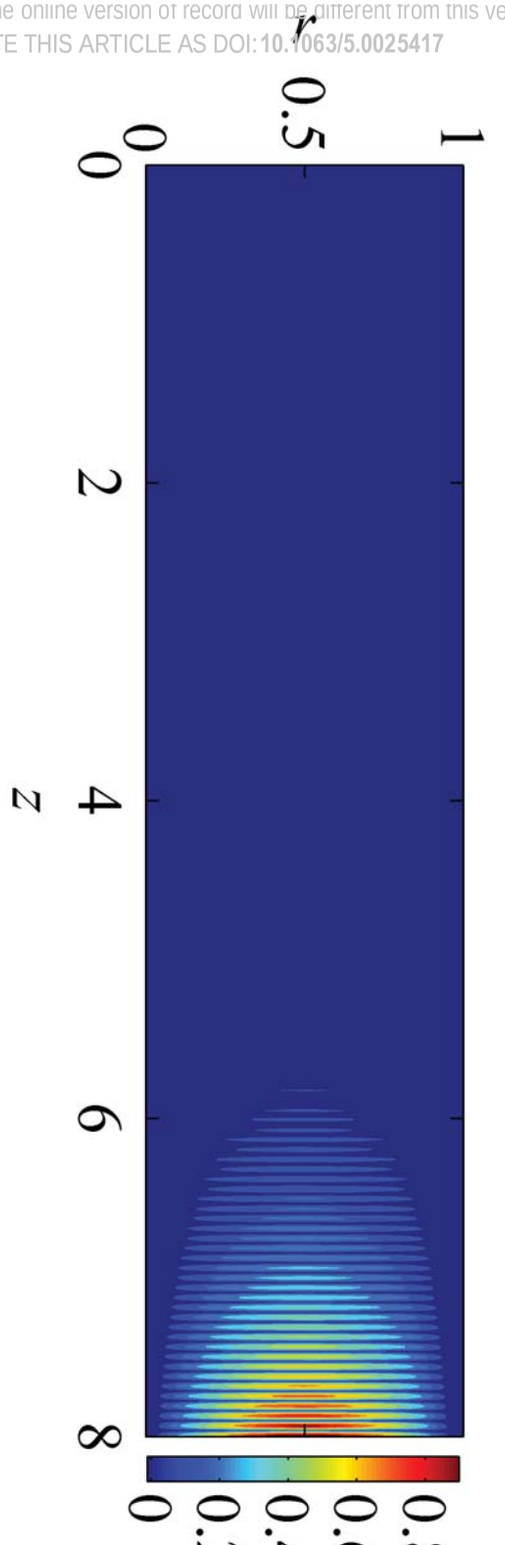

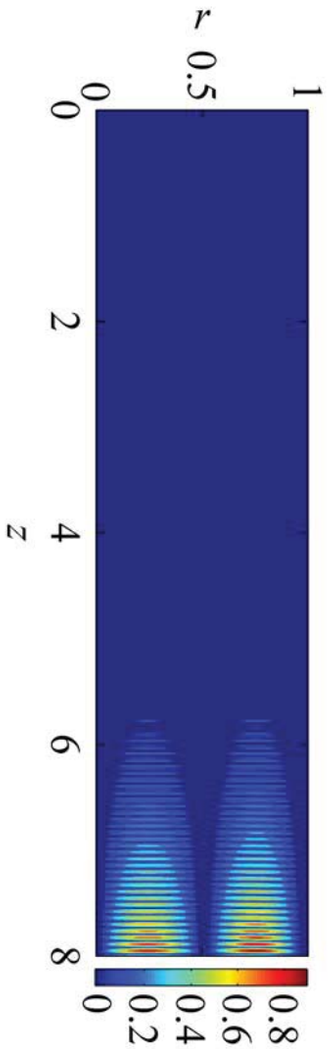

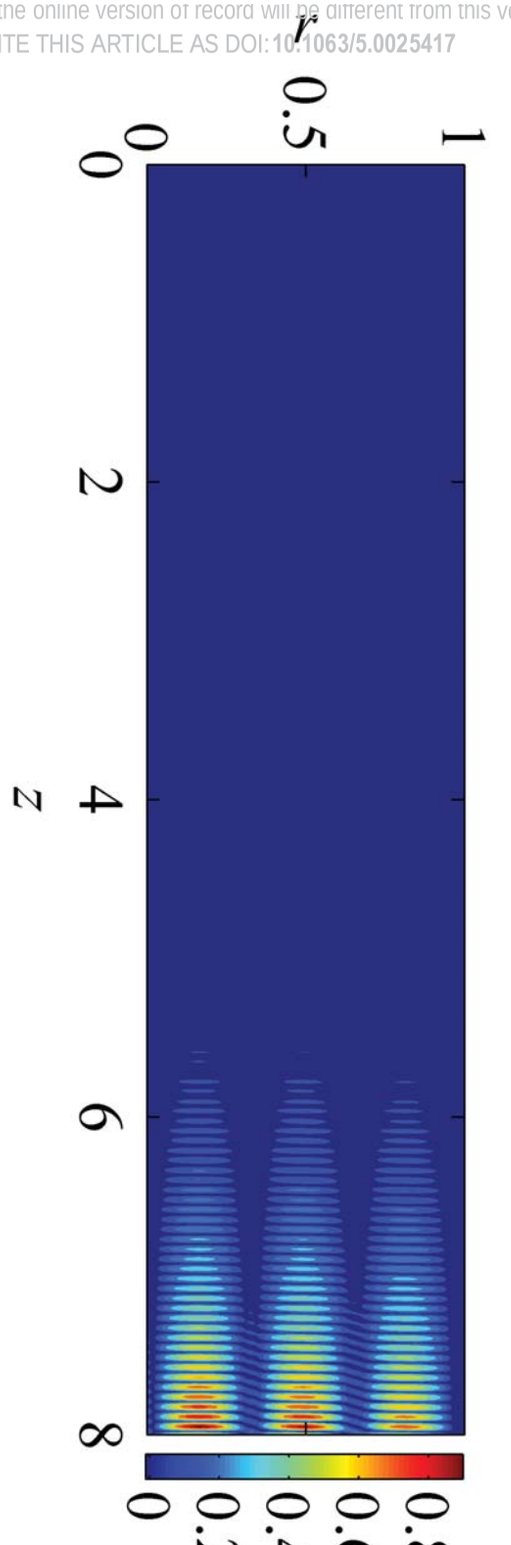

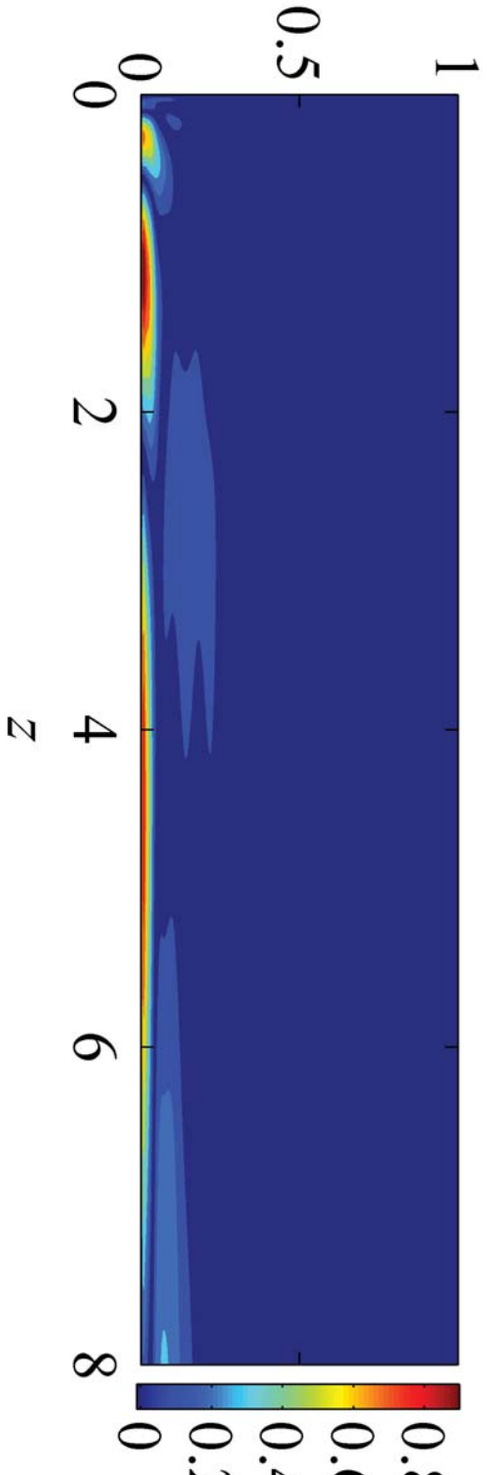

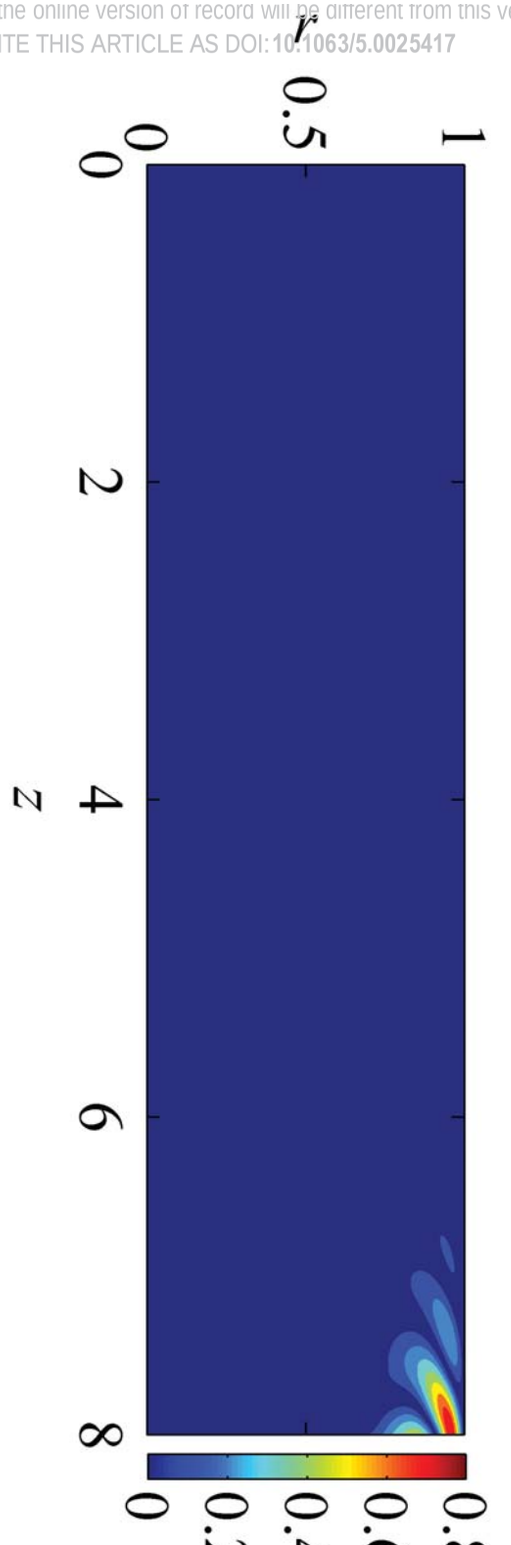

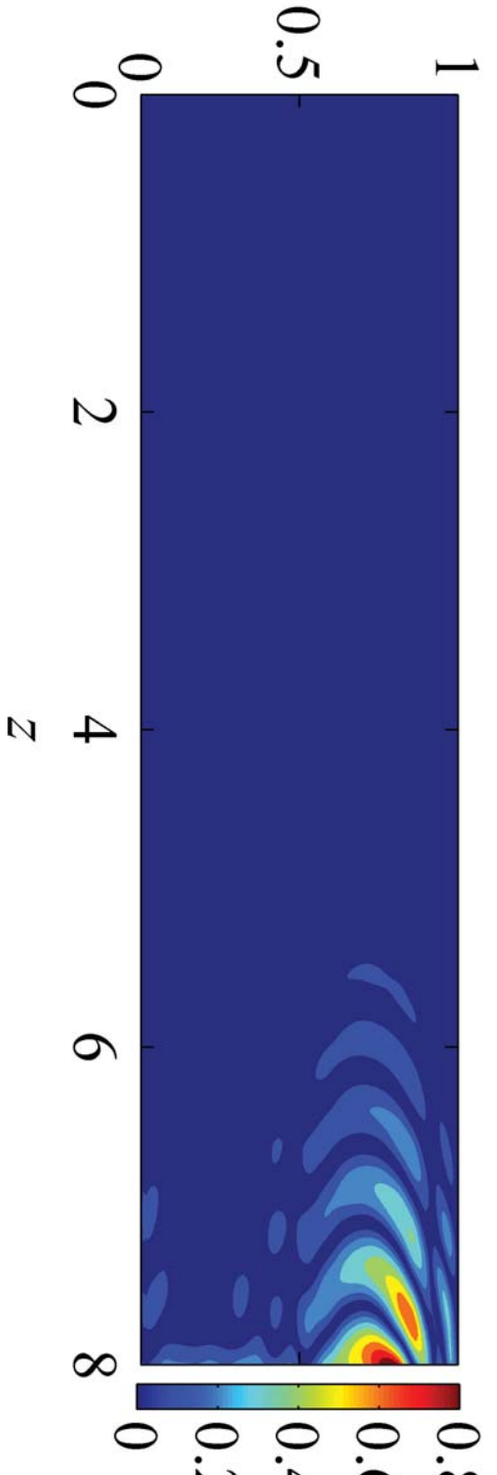

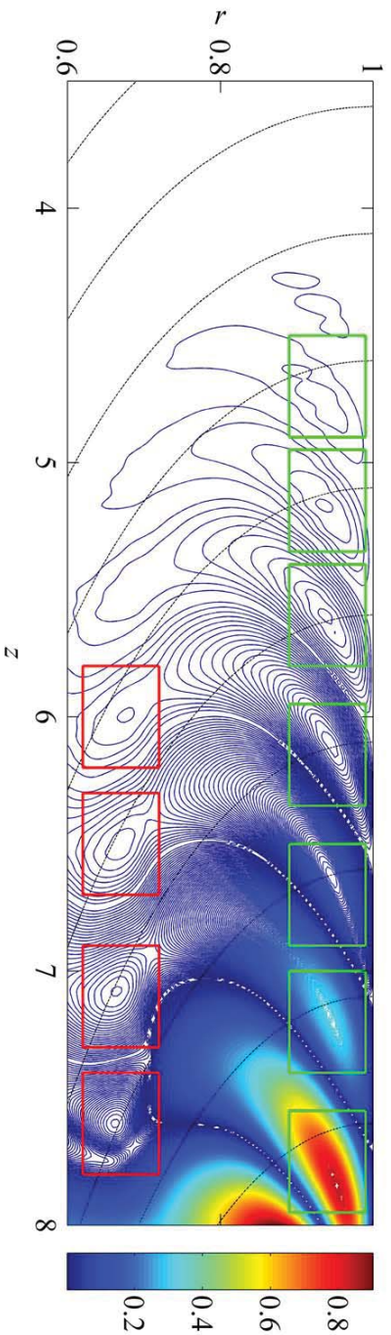

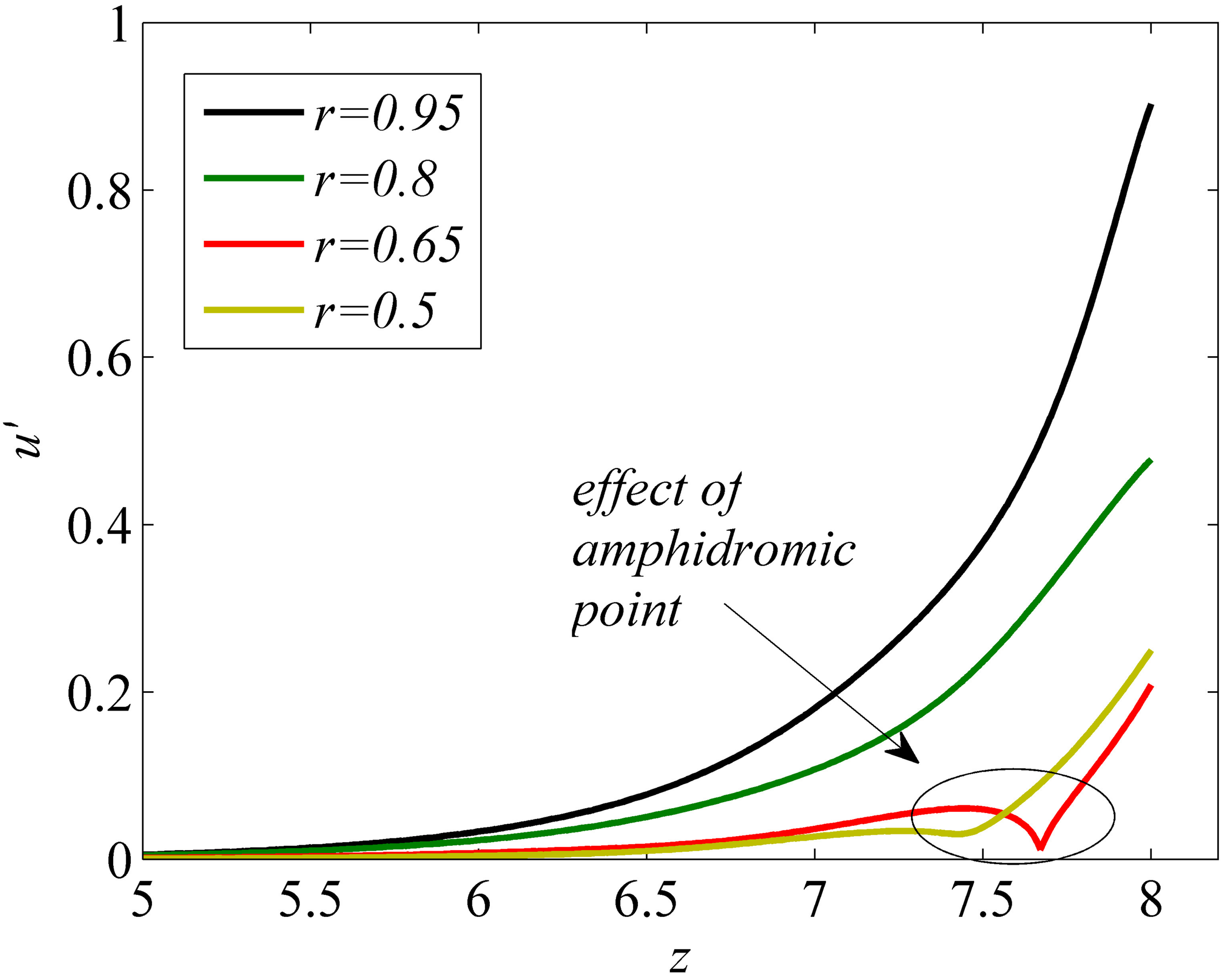
r=0.95
r=0.8
r=0.65
r=0.5
effect of
amphidromic
point
u'
z
1
0.8
0.6
0.4
0.2
0
5
5.5
6
6.5
7
7.5
8

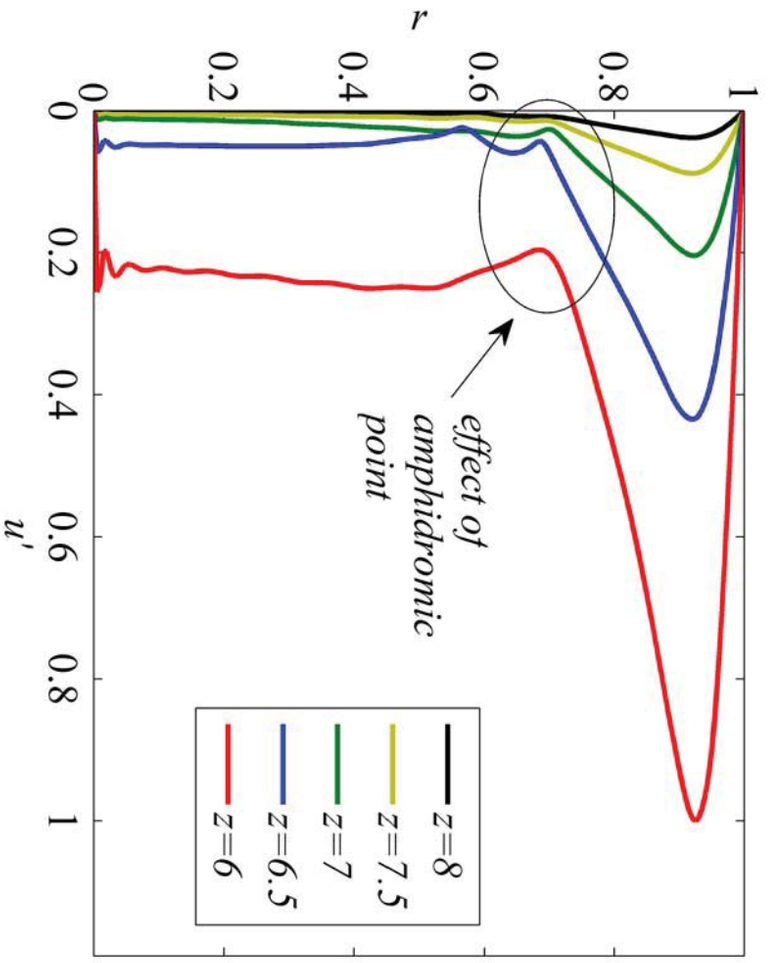

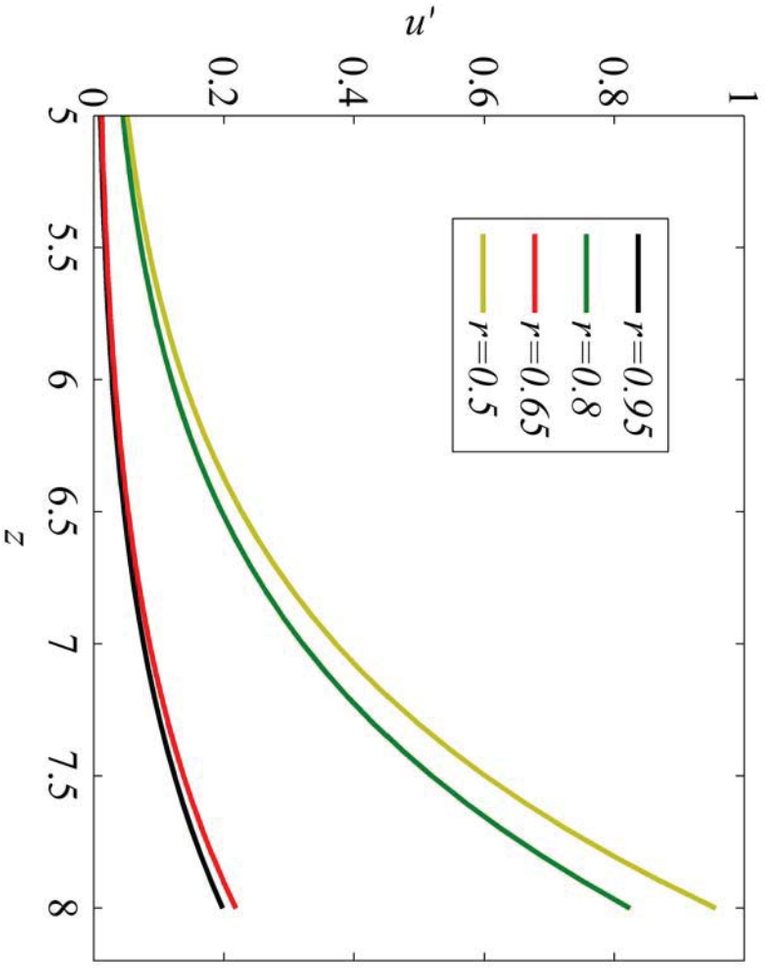

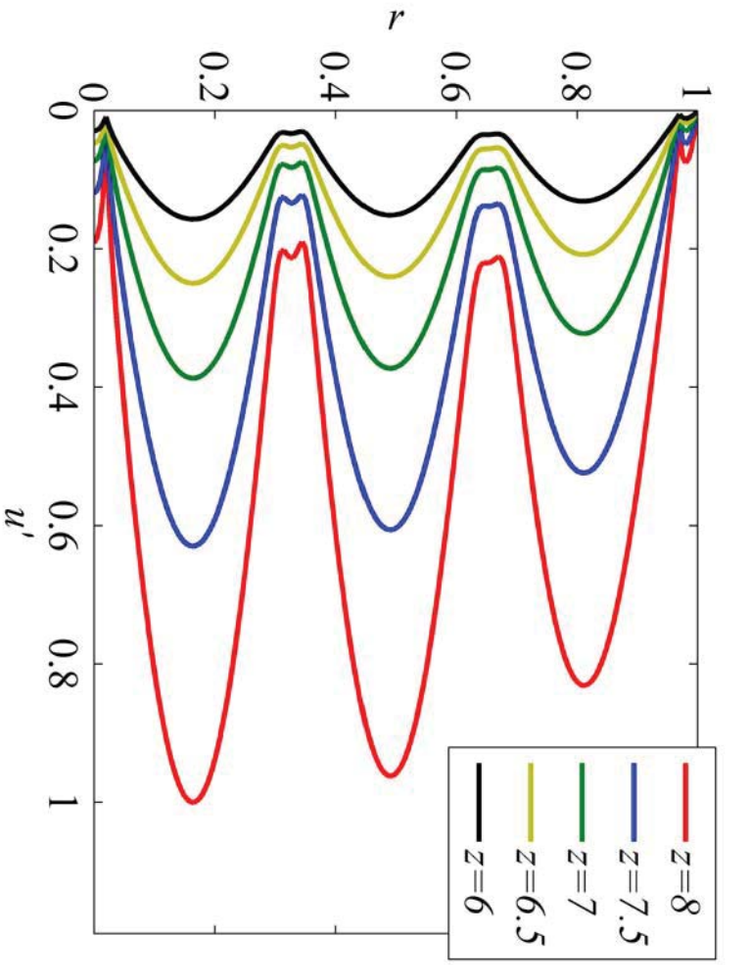

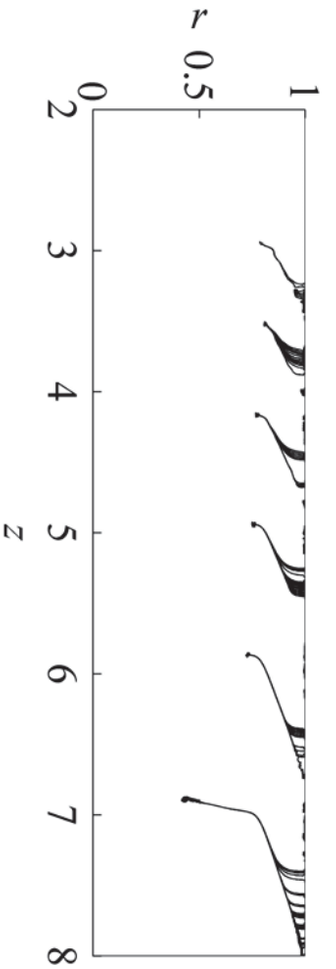

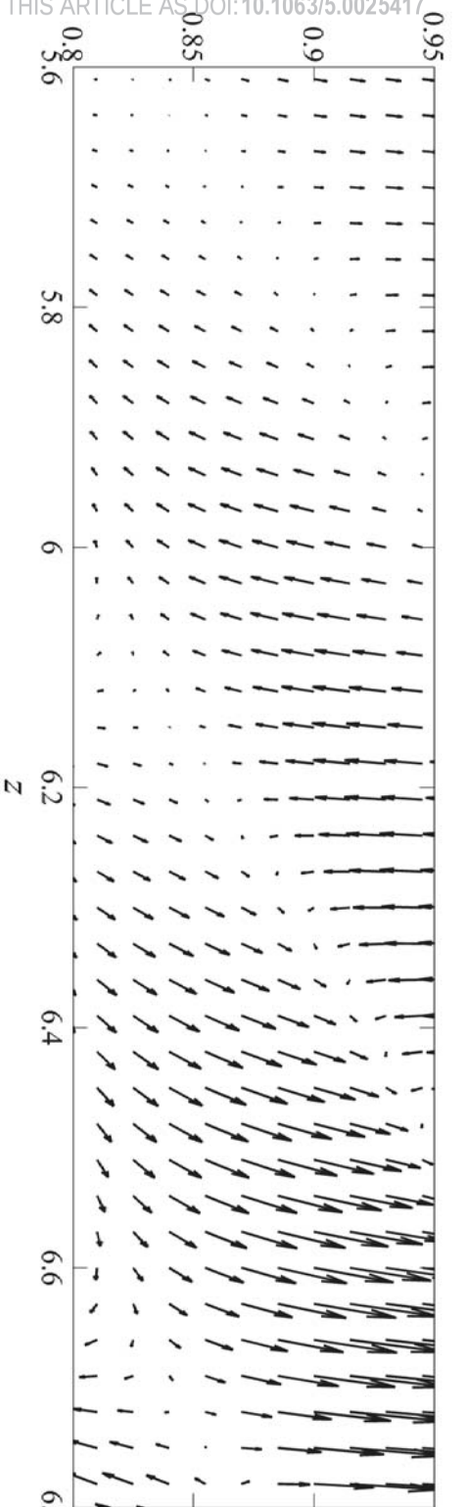

PLEASE CITE THIS ARTICLE AS DOI: 10.1063/5.0025417